LBL-24796 c.2
UC-11

Lawrence Berkeley Laboratory
UNIVERSITY OF CALIFORNIA

EARTH SCIENCES DIVISION

Estimating Properties of Unsaturated Fractured Formations from Injection and Falloff Tests

S. Mishra, G.S. Bodvarsson,
and M.P. Attanayake

December 1987

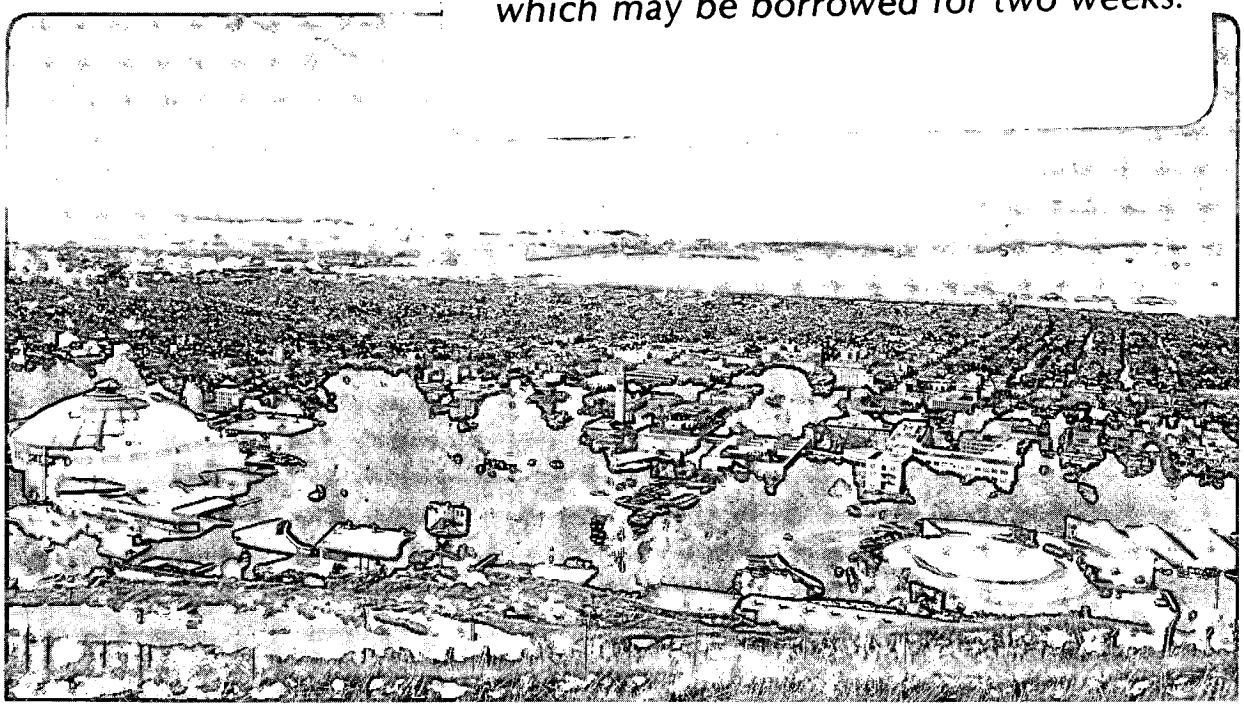

Prepared for the U.S. Department of Energy under Contract DE-AC03-76SF00098

DISCLAIMER

LBL-24796

Estimating Properties of Unsaturated Fractured Formations from Injection and Falloff Tests

S. Mishra, G.S. Bodvarsson and M.P. Attanayake

Earth Sciences Division
Lawrence Berkeley Laboratory
University of California
Berkeley, California 94720

ABSTRACT

A new technique for calculating hydraulic properties of unsaturated fractured formations is proposed as an alternative to the common approach involving steady-state analysis of multi-rate gas injection tests. This method is based on graphical analysis of unsteady-state pressure-time data from an injection-falloff test sequence. Both gas and water injection testing are considered. Flow in a horizontal fracture of limited lateral extent, bounded above and below by an impermeable matrix, and intersected by a cylindrical borehole is described by two analytical models developed in this study. The first model corresponds to the early-time infinite acting radial flow period, and the second to the late-time linear flow period. Interpretive equations are derived for computing fracture conductivity and volumetric aperture from early-time pressure data, and fracture width from late-time pressure data. Effects of fracture inclination and gravity are studied numerically and found to be practically negligible for gas as well as water injection. Two simulated injection-falloff tests are analyzed using the suggested procedure. Results are found to be in good agreement with simulator input values.

Introduction

The possibility of siting high-level nuclear waste repositories in unsaturated fractured formations has generated interest in developing characterization procedures for such media. Fractures are high-conductivity flow channels forming a network of conduits through which fluid(s) can flow. From a hydrogeologic standpoint, the properties of major interest in these systems are fracture conductivity, spacing, orientation and aperture. For plane fractures of limited extent in the lateral direction, the width is also an important parameter.

Hydraulic properties of fractures such as conductivity and aperture are usually measured in an indirect manner, with some type of flow test. The most common approach involves injecting gas into a packed-off section of a borehole which intersects the fracture(s) of interest. Gas is injected at a series of flow rates, and the stabilized pressure corresponding to each rate is measured. Permeability (or equivalently, hydraulic conductivity) is calculated from the appropriate steady-state solution of the pressure diffusion equation (Montazer, 1982; Trautz, 1986). Such a solution typically relates mass rate q_m to the pressure drop between the injection borehole and some observation point expressed as Δp^2 through a constant of proportionality which includes conductivity.

Montazer (1982) conducted an extensive experimental study of in-situ permeability measurements using such techniques and identified three major effects which affect the injection test response. These are (a) the Klinkenberg effect (Klinkenberg, 1941), (b) interference effects and (c) the unsaturated nature of the rock. The Klinkenberg effect refers to the slippage between gas molecules and pore walls at low pressures, which results in an apparent increase in permeability. This pressure dependence can be accounted for by measuring permeability at a range of pressure, and then extrapolating the linear pressure-permeability trend to infinite pressure so as to obtain the liquid permeability. Montazer (1982) found that it was necessary to conduct multi-rate injection tests in order to calculate the absolute (liquid) permeability because of this phenomenon.

He also observed that the pressure-permeability relationship may exhibit non-linearities because pressure gradients from one rate may interfere with new gradients which are created when rates are changed. These may be compounded by capillary and slip effects, which arise due to unsaturated conditions in the fracture.

Trautz (1984) used steady-state gas injection tests to measure gas conductivities of fractures in an unsaturated igneous rock. He developed equations for computing permeability from flow tests in elliptical flow situations which are created when plane inclined fractures intersect vertical cylindrical boreholes. He observed that non-linear effects may be created under unsaturated conditions because of water blockage.

In this study, we explore the alternative approach of using unsteady-state pressure data from injection and falloff tests. This method involves injecting a fluid into a formation for a period of time, and then shutting the borehole to allow pressure to falloff. Graphical analysis of transient pressure-time data yields formation permeability, distance to linear barriers (such as lateral fracture boundaries) and formation pressure at initial conditions. Such techniques have been widely used for estimating hydraulic properties of saturated groundwater aquifers (Witherspoon et al., 1967), oil and gas reservoirs (Earlougher, 1977) and geothermal systems (Grant et al., 1982).

There are several advantages of using transient testing methods when compared to steady-state techniques. A steady-state test has to be conducted at several rates, and stabilized pressures measured at the injection well and an observation well for each rate. Care has to be taken so that non-linear effects do not dominate the test when rates are changed. The onset of stabilization (i.e., steady-state conditions) can only be estimated crudely. Moreover, geometrical parameters such as volumetric (tracer) aperture and fracture width cannot be estimated form steady-state testing alone.

It is important to distinguish between the hydraulic aperture h and the volumetric aperture h_{vol}. The former is estimated from a relationship between permeability and permeability-thickness (transmissivity) and aperture (see Appendix C).

$$(kh) = 8.3 \times 10^6 \, h^3 \qquad (1)$$

whereas the volumetric aperture is obtained from material balance considerations.

$$qt = \pi r^2 \phi \Delta sh_{vol} \quad (1)$$

If the fracture is visualized as a system containing several sections of varying apertures, the hydraulic aperture can be thought of as a parameter representing the effective conductance, whereas the volumetric aperture represents the average pore space for fluid flow.

This report deals with the development of analytical models which describe pressure behavior in unsaturated fractures during injection-falloff. Interpretive equations are derived for computing fracture properties from analysis of pressure-time data. Effects of fracture inclination and gravity are investigated. Example analyses of simulated injection-falloff tests are presented.

Mathematical Model

In this section we describe the physical system of interest and state the assumptions made in formulating the mathematical model. Based on the solution to this model, we then derive equations for analyzing injection and falloff pressure data. The basic premises of this discussion are as follows.

(a) Flow takes place in a plane natural fracture which is inclined at some angle to the horizontal, and intersected by a cylindrical borehole (Fig 1). In our theoretical treatment, we assume that the fracture is horizontal and gravity effects are negligible. The effects of fracture inclination and gravity will be investigated numerically, and discussed later.

(b) The fracture has constant width and aperture, and is bounded above and below by an impermeable matrix. Initially, the fracture is unsaturated, i.e., it contains a two-phase mixture of water and air. Following Perrine (1956), we assume that single-phase flow equations can be used to describe two-phase flow conditions if the total mobility (sum of the individual phase mobilities) is substituted for single-phase mobility, where mobility $\lambda = k/\mu$.

(c) During injection, the injected fluid displaces the formation fluids in a piston-like manner and a sharp moving front develops in the system. The presence

of this moving front creates a mobility contrast between the inner (invaded) and the outer (uninvaded) zones. The moving front, which separates these two zones, moves at a constant areal velocity during the injection period. Upon the completion of injection (i.e., during the falloff period) the front is stationary.

(d) Wellbore storage and skin effects are neglected.

It is useful to conceptualize the temporal development of flow in the fracture during injection. At early times, before either the pressure or the saturation front has reached the lateral boundaries of the fracture, flow will be radial. The boundary between the two fluid zone will move in the form of radially concentric circles during this period. Once the effect of the lateral boundaries have been felt, the flow regime will gradually change from radial to linear. At late times, the borehole will behave like a plane source and both pressure and saturation fronts will move in a linear fashion. This corresponds to a linear flow period (see Fig. 1(b)). The existence of such distinct flow regimes at early and late times suggests that two separate solutions may be superimposed to describe the flow behavior approximately. Based on this rationale, we have developed an interpretation model which combines the early-time radial flow solution with the late-time linear flow solution.

All derivations in this section will be presented for the case of gas injection. However, the final solution will be expressed in dimensionless form, and hence should apply to liquid systems (i.e., water injection) as well when appropriate dimensionless variables are defined and used. In deriving the flow equations, it will be assumed that the gas is ideal. Furthermore, an average pressure $\overline{p}$ will be used to convert derivative of p to derivatives of p^2 so that the flow equations are linearized. The proper choice of $\overline{p}$ is discussed in a later section.

Early-time Radial Flow

The partial differential equations governing the pressure response during this period, together with initial and boundary conditions, and the method of solution are given in Appendix A. Here, we present the results in dimensionless form, and derive working equations. All equations are written in consistent darcy (CGS) units. Similar solutions, for liquid flow in composite media, have been given by Ramey (1970) and Woodward and Thambynayagam (1983).

(a) Injection Pressure Response

The dimensionless wellbore during injection is given by

$$p_{wD} = \frac{\pi\lambda_1 h}{q\bar{p}}(p_{wf}^2 - p_i^2) = \frac{1}{2}\,\mathrm{Ei}\left(-\frac{1}{4t_D}\right) + \frac{M}{2}\,\mathrm{Ei}\left(-\frac{aD}{4}\right)\cdot\exp\left(-\frac{a(1-D)}{4}\right) - \frac{1}{2}\,\mathrm{Ei}\left(-\frac{a}{4}\right) \tag{3}$$

At early times, when $t_D > 10$, the log approximation to the exponential integral holds, i.e., $\mathrm{Ei}(-x) = \ln(\gamma x)$, and Eq. (3) reduces to

$$p_{wD} = \left[\frac{1}{2}\ln(t_D) + 0.405\right] + S \tag{4}$$

This is identical to the line-source solution in an infinite radial system (Earlougher, 1977), but with an additional dimensionless pressure drop or skin caused by the moving front, expressed as

$$S = \frac{M}{2}\,\mathrm{Ei}\left(-\frac{aD}{4}\right)\cdot\exp\left(-\frac{a(1-D)}{4}\right) - \frac{1}{2}\,\mathrm{Ei}\left(-\frac{a}{4}\right) \tag{5}$$

Substituting for dimensionless variables, one obtains from Eq. (4)

$$p_{wf}^2 - p_i^2 = \frac{1.151 q\bar{p}}{\pi\lambda_1 h}\left\{\log\frac{t}{r_w^2} + \log\eta_1 + \frac{S+0.405}{1.151}\right\} \tag{6}$$

Eq. (6) suggests that a graph of p_{wf}^2 against log (t) should produce a straight line with slope

$$m_1 = \frac{1.151 q\bar{p}}{\pi \lambda_1 h} \tag{7}$$

from which the mobility thickness $\lambda_1 h$ of the inner zone can be calculated. Moreover, if the skin due to the moving front is known, the inner zone diffusivity can be calculated from

$$\log \eta_1 = \left\{ \frac{p_{wf}^2 \Big|_{\frac{t}{r_w^2}=1} - \left(p_i^2 + \frac{m_1 S}{1.151} \right) - 0.352\, m_1}{m_1} \right\} \tag{8}$$

(b) Falloff Pressure Response

The falloff response can be computed from the injection response using superposition. Defining a dimensionless shut-in pressure

$$p_{DS} = \frac{\pi \lambda_1 h}{q\bar{p}} (p_{ws}^2 - p_i^2) = p_{wD}\,(t_{pD} + \Delta t_D) - p_{wD}(\Delta t_D) \tag{9}$$

and substituting from Eq. (3), we have

$$p_{DS} = \left[\frac{1}{2} \mathrm{Ei}\left(-\frac{1}{4(t_{pD}+\Delta t_D)} \right) + \frac{M}{2} \mathrm{Ei}\left(-\frac{aDt_{pD}}{4(t_{pD}+\Delta t_D)} \right) \cdot \exp\left(-\frac{a(1-D)t_{pD}}{4(t_{pD}+\Delta t_D)} \right) \right.$$
$$\left. - \frac{1}{2} \mathrm{Ei}\left(-\frac{at_{pD}}{4(t_{pD}+\Delta t_D} \right) \right] - \left[\frac{1}{2} \mathrm{Ei}\left(-\frac{1}{4\Delta t_D} \right) + \frac{M}{2} \mathrm{Ei}\left(-\frac{aDt_{pD}}{4\Delta t_D} \right) \right.$$
$$\left. \cdot \exp\left(-\frac{a(1-D)t_{pD}}{4\Delta t_D} \right) - \frac{1}{2} \mathrm{Ei}\left(-\frac{at_{pD}}{4\Delta t_D} \right) \right] \tag{10}$$

Consider the fall-off response for $t_{pD} >> \Delta t_D$. Eq. (10) can than be simplified to

$$p_{DS} = \frac{1}{2} \mathrm{Ei}\left(-\frac{1}{4(t_{pD}+\Delta t_D)} \right) - \frac{1}{2} \mathrm{Ei}\left(-\frac{1}{4\Delta t_D} \right) + \frac{M}{2} \mathrm{Ei}\left(-\frac{a\bar{D}}{4} \right) \cdot \exp\left(-\frac{a(1-D)}{4} \right)$$
$$- \frac{1}{2} \mathrm{Ei}\left(-\frac{a}{4} \right) - \frac{M}{2} \left(-\frac{aDt_{pD}}{4\Delta t_D} \right) - \exp\left(-\frac{a(1-D)t_{pD}}{4\Delta t_D} \right) - \frac{1}{2} \mathrm{Ei}\left(-\frac{at_{pD}}{4\Delta t_D} \right) \tag{11}$$

Furthermore, if the log approximation to the exponential integral applies, Eq. (11)

reduces to

$$p_{DS} = \frac{1}{2} \ln \left(\frac{t_{pD} + \Delta t_D}{\Delta t_D} \right) + S \tag{12}$$

This can be rewritten in terms of real variables as

$$p_{ws}^2 - p_i^2 = \frac{1.151 q\overline{p}}{\pi \lambda_1 h} \left\{ \log \left(\frac{t_p + \Delta t}{\Delta t} \right) + \frac{S}{1.151} \right\} \tag{13}$$

Thus, a conventional Horner graph (Horner, 1951) of p_{ws}^2 versus $\log (t_p + \Delta t)/(\Delta t)$ should also yield a straight line of slope

$$m_1 = \frac{1.151 q\overline{p}}{\pi \lambda_1 h} \tag{14}$$

from which $\lambda_1 h$ can be calculated. Also, by extrapolating to a Horner time ratio of unity, one can compute

$$p_{ws}^2 \Big|^* = p_i^2 + \frac{m_1 S}{1.151} \tag{15}$$

The group in the right is needed to evaluate the inner zone diffusivity η_1 from Eq. (8).

The semi-log straight line, defined by Eq. (12), will end when

$$\mathrm{Ei} \left(-\frac{a t_{pD}}{4 \Delta t_D} \right) \neq 0 \tag{16}$$

For practical purposes, this implies

$$\mathrm{Ei} \left(-\frac{a t_{pD}}{4 \Delta t_D} \right) \approx 0.10 = \mathrm{Ei}^{-1} (1.5) \tag{17}$$

which can be rearranged to give

$$a = \frac{6}{\left\{ \left(\frac{t_p + \Delta t}{\Delta t} \right)^{**} - 1 \right\}} \tag{18}$$

where $\left\{ (t_p + \Delta t)/(\Delta t) \right\}^{**}$ is the time at which the early-time Horner straight line approximately ends. Now, from Eq. (A.39)

$$a = \frac{q}{\pi h_{vol}\, \phi \Delta s \eta_1} \tag{19}$$

since the diffusivity η_1 is evaluated from Eq. (8), the volumetric fracture aperture h_{vol} can be estimated from

$$h_{vol} = \frac{q}{\pi a \phi \Delta s \eta_1} \tag{20}$$

Thus, Eqs. (7) or (14), (8) and (20) provide a simple scheme for calculating the mobility-thickness of the inner zone, the diffusivity of the inner zone and the fracture aperture respectively. Since the viscosity of the injected fluid will be known, the permeability-thickness k_1h of the inner zone can be estimated from the mobility thickness $\lambda_1 h$. The hydraulic aperture can then be calculated from Eq. (1).

At late time, if $\Delta t_D >> t_{pD}$ and both are large such that the log approximation holds, Eq. (10) simplifies to

$$p_{DS} = \frac{M}{2} \ln\left(\frac{t_{pD} + \Delta t_D}{\Delta t_D}\right) \tag{21}$$

or, in terms of real variables,

$$p_{ws}^2 - p_i^2 = \frac{1.151 q \bar{p}}{\pi \lambda_2 h} \log\left(\frac{t_p + \Delta t}{\Delta t}\right) \tag{22}$$

This indicates that the intermediate (middle-time) fall-off data will produce a Horner straight line of slope

$$m_2 = \frac{1.151 q \bar{p}}{\pi \lambda_2 h} \tag{23}$$

from which the mobility thickness of the outer zone can be calculated.

Late-Time Linear Flow

Appendix B outlines the formulation of the linear moving-front problem, and its approximate solution. The later time injection pressure is given by

$$p_{wD}^* = 2M \sqrt{\frac{t_D^*}{\pi D}} \tag{24}$$

or, in terms of real variables

$$p_{wf}^2 - p_i^2 = \frac{1.128q\overline{p}}{\lambda_2 bh}\sqrt{\eta_2 t} \tag{25}$$

The falloff response, using superposition, is obtained as

$$p_{DS}^* = \frac{2M}{\sqrt{\pi D}}\left\{\sqrt{t_{pD}^* + \Delta t_D^*} - \sqrt{\Delta t_D^*}\right\} \tag{26}$$

or, in terms of actual parameters,

$$p_{wS}^2 - p_i^2 = \frac{1.128q\overline{p}}{\lambda_2 bh}\sqrt{\eta_2}\left\{\sqrt{t_p + \Delta t} - \sqrt{\Delta t}\right\} \tag{27}$$

These solutions can be used to calculate the fracture width b if outer zone properties λ_2 and η_2 can be estimated. From Eq. (25) and (27), we see that cartesian graphs of injection pressure p_{wf}^2 versus injection time t, or falloff pressure p_{ws}^2 versus the time group $\sqrt{(t_p+\Delta t)} - \sqrt{(t)}$, will yield a straight line with intercept equal to the square of the initial pressure, and slope

$$m_3 = \frac{1.128\ q\overline{p}\sqrt{\eta_2}}{\lambda_2 bh} \tag{28}$$

The fracture width b can then be calculated from this equation.

Linearization of Gas Flow Equations

The p^2 formulation is one way of linearizing the non-linear gas flow equations, provided the pressure level and pressure changes are small. A proper value of $\overline{p}$ then needs to be selected to calculate fracture properties using their interpretive equations derived in the previous section. In order to determine the proper average, three injection tests for the same system but with different injection rates were simulated. The numerical tool used was TOUGH (Pruess, 1985), a program to simulate two-phase two-component flow of water and air. The objective was to find the appropriate $\overline{p}$ (and corresponding $\overline{\rho}$ and $\overline{\mu}$) for which the permeability calculated from the slope of the injection semi-log graph is approximately equal to the simulator input value.

Table 1
Summary of Permeability Calculations
Linearization of Gas Flow Equation Example

Case	q_m (kg/s)	m (atm/≈)	$\overline{p}$ (atm)	ρ (kg/cc)	q (cc/s)	$\overline{\mu}$ (cp)	k (darcy)
1	2.48×10^{-5}	0.273	1.019	1.26×10^{-6}	19.7	0.018	4.86
2	2.48×10^{-4}	0.274	1.301	1.66×10^{-6}	149.7	0.0185	4.82
3	1.48×10^{-3}	0.270	2.992	3.70×10^{-6}	670.0	0.021	5.65

System Data: p_i (Pa) $= 10^5$, T(°C) = 10, k (darcy) = 5, h(cm) = 1, r_w (cm) = 10, $S_{gi} = 0.97$, $S_{wi} = 0.03$.

Table 2
Effect of Fracture Inclination on Wellbore Pressure Reponse During Gas Injection

t (sec)	P_{wf} (α=0°) (10^5Pa)	P_{wf} (α=30°) (10^5Pa)
1	1.13169	1.13169
2	1.21904	1.21904
16	1.28812	1.28812
64	1.35045	1.35038
128	1.38225	1.38189
512	1.46716	1.46509
1280	1.56263	1.55912
2304	1.65107	1.64696
3154	1.70961	1.70607

System: p_i (Pa) = 10^5, T(°C) = 10, K (darcy) = 5, h (cm) = 1, r_w (cm) = 10, s_{gi} = 0.97, s_{wi} = 0.03.

Table 3
Effect of Gravity on Wellbore
Pressure Response During Water Injection

$q_m = 1.4 \times 10^{-3}$ kg/s			$q_m = 4 \times 10^{-3}$ kg/s			$q_m = 4 \times 10^{-2}$ kg/s		
	p_{wf} (10^5 Pa)			p_{wf} (10^5 Pa)			p_{wf} (10^5 Pa)	
t (sec)	α=0°	α=60°	t (sec)	α=0°	α=30°	t (sec)	α=0°	α=60°
15	1.00217	1.00216	18	1.00590	1.00589	10	2.02106	2.02105
31	1.00248	1.00247	23	1.00688	1.00687	24	2.80513	2.80512
63	1.00276	1.00276	55	1.02631	1.02625	60	3.73703	3.73702
127	1.00314	1.00313	111	1.09659	1.09648	108	4.33621	4.33592
319	1.01865	1.01855	275	1.17773	1.17758	236	4.99936	4.99856
735	1.04822	1.04811	625	1.27140	1.27119	620	6.21492	6.20643
1220	1.06508	1.06490	1140	1.32618	1.32520	1004	6.88306	6.85386
4350	1.11757	1.11450	2419	1.38797	1.38299	2284	6.8836	6.85386
			5482	1.46581	1.45895	5868	7.81970	7.81672
8000	1.13589	1.12905	10000	1.49809	1.48723	10476	8.37960	8.18227

Other Data: $k = 5D$, $\mu = 1.3$ cp, $\phi = 0.50$, $p_i = 10^5$ Pa, $r_w = 10$ cm, $h = 1$ cm, $b = 10$ m, $S_{wi} = 0.03$, $T = 10\,^{\circ}$C, $\rho = 10^3$ kg/m^3

Table 4
Model Validation

System Data	
p_i (Pa)	10^5
T (°C)	10
k (darcy)	5
h	1 (cm)
r_w (cm)	10
S_{gi}	0.50
S_{wi}	0.50
Air-Injection Test Parameters	
q_m (gas)	4.96×10^{-5} kg/s
t_p	300 sec
Δt_{max}	3300 sec
Water-Injection Test Parameters	
q_m (water)	4×10^{-3} kg/s
t_p	20000 sec
Δt_{max}	180000 sec

Figures 2 through 4 show injection pressure responses corresponding to the three different injection rates. By examining these graphs, we found that the proper average pressure is the average during the infinite acting radial flow period (corresponding to the semi-log straight line). As long as pressure changes are below approximately 2 atm., this rule gives quite good answers. However, for greater rates and hence large pressure changes (e.g., Fig. 4), the well response becomes nonlinear and continuously changes slope on the semi-log graph. If a semi-log straight line is nevertheless drawn through the point of inflection (point Δ on Fig. 4), and the corresponding pressure chosen as the average pressure, errors larger than 10% may be expected in permeability calculations. Table 1 summarizes permeability calculations for the three different cases studied.

Effects of Fracture Inclination

When flow in an inclined fracture is modeled, two additional factors need to be considered. Because of the altered flow geometry (cylindrical borehole and inclined fracture), early-time flow may no longer be radial, as in a horizontal fracture. Moreover, the influence of gravity forces vis-a-vis viscous forces has to be taken into account. These effects are discussed below.

Modifications in Flow Geometry

When an inclined fracture is intersected by a cylindrical borehole (as in Fig. 1a), the resulting conic section is an ellipse and the flow geometry is elliptical rather than radial. Trautz (1984) derived steady-state elliptical flow solution to compute gas conductivity in natural fractures which are inclined and used these to interpret data from field tests. However, in his extensive study on transient flow in elliptical systems, Kucuk (1978) showed that any elliptical flow system can be converted to an equivalent radial system after a certain dimensionless time t_{Dr}, which is graphed in Figure 5 as a function of a/b, the ratio of the semi-major axis of the ellipse to the semi-minor axis. Here

$$\frac{a}{b} = \sec \alpha \tag{29}$$

$$r_w' = r_w \tan\alpha \, \frac{0.5(\frac{a}{b}+1)}{\sqrt{(\frac{a}{b})^2-1}} \tag{30}$$

$$t_{Dr} = \frac{kt\overline{p}}{(\phi\mu r_w'^2)} \tag{31}$$

where α is the inclination of the fracture with respect to the horizontal, and r_w is the actual wellbore radius. For most practical situations, the onset of radial flow occurs at very early times. As an example, for the case of air injection, if k = 5 darcy, $\overline{p}$ = 1 atm, μ = .018 cp, ϕ = 0.50, r_w = 10 cm, and $\alpha = 60°$,

a/b = 2, t_{Dr} = 20 (Fig. 5), r_w' = 15 cm (Eq. 30), t = 8 sec (Eq. 31). Thus, after about eight seconds of injection, the system will behave like a radial flow system for all practical purposes. Hence, it is reasonable to assume that elliptical flow effects can be modeled by radial flow equations for all times of interest.

Gravitational Effects

In highly unsaturated fractures (i.e., with very low water saturations) which are inclined, the initial (static) pressure distribution will be nearly uniform because of negligible gravitational potential of gas. Once injection begins, the amount of injected fluid going updip and downdip can be approximated by:

$$q_{up} = -\pi\lambda_1 h \left\{ \frac{\partial p}{\partial(\ln r)} + \frac{\rho g r_w \sin\alpha}{1.0133 \times 10^6} \right\} \tag{32}$$

$$q_{down} = -\pi\lambda_1 h \left\{ \frac{\partial p}{\partial(\ln r)} - \frac{\rho g r_w \sin\alpha}{1.0133 \times 10^6} \right\} \tag{33}$$

In the case of gas injection, the gravitational component will usually be much smaller than the flow rate induced pressure gradient, since the density of gas is very small. This will result in almost equal amounts being injected updip and downdip, and consequently gravity effects on the pressure transient response will be negligible.

An injection test was simulated using TOUGH (Pruess, 1985) to study the effects of gravity when gas is used as the injection fluid in an inclined fracture. Table 2 lists the system data and the injection response for this case, as well as that for the corresponding horizontal fracture case. The maximum difference in observed pressures was less than 1%, indicating that gravitational effects were negligible. This is consistent with the

expected behavior as discussed above.

For the case of water injection, the dynamic distribution of fluids in updip and downdip directions will depend on the relative magnitudes of the pressure gradient and the gravitational terms. Since the pressure gradient is affected by the injection rate, one would expect gravity effects to be dominant primarily at low rates (small pressure gradients). We simulated water injection tests at three different rates to investigate this phenomenon. Table 3 lists system data, and pressure responses for the various cases studied.

In all the cases, the difference in the inclined and horizontal fractured system behavior was observed to be very small. This is believed to be due to large flow rate induced pressure gradients created in the system. In fact, calculation of this pressure gradient showed that it was at least two orders of magnitude higher than the gravitational term even for the smallest rate. A practical implication is that in most situations where fractures are included, even small rates will lead to large pressure gradients in the system (because of small apertures) which will dominate the gravitational effects. Hence, errors in analyzing transient pressure data from inclined fractures using interpretative equations derived for horizontal fractures will usually be small.

Model Verification

Two simulated injection-falloff test sequences were analyzed using the methods developed in this study as a verification exercise. Pressure-time data for an air-injection test and a water-injection test were simulated with TOUGH (Pruess, 1985). Because of the symmetry in the system, flow in one quarter of the fracture (Fig. 1b) was simulated. In order to obtain reasonable resolution in the near-wellbore region, a radial grid was used till a distance of 5 m. Further away from the well rectangular elements were used to a total system dimension of 674.5 m. This system size was sufficient so that the effects of outer boundary would not be felt during the simulation period of interest. Such a hybrid grid arrangement is facilitated by the integral finite difference formulation (IFDM) used in TOUGH. Grid spacing was logarithmic for accurate modeling of

transient pressure response. A total of 65 elements was used in the flow domain.

Conventional Steady-State Analysis of Injection Test Data

For comparative purposes, we include an analysis of the injection test pressure data using steady-state equations. Cartesian graphs of pressure time data are given in Fig. 6 and 7. Following Montazer (1982), we write the steady-state flow equation for gas injection as

$$kh = \frac{q_m \mu RT}{\pi \rho M} \cdot \frac{\ln(r_e/r_w)}{(p_w^2 - p_e^2)} \tag{34}$$

where R is the universal gas constant, M the molecular weight of the gas, T the absolute temperature, p_w the steady-state injection pressure, and p_e the boundary pressure at radius r_e. Similarly, the equation for water injection is

$$kh = \frac{q_m \mu}{2\pi \rho} \cdot \frac{\ln(r_e/r_w)}{(p_w - p_e)} \tag{35}$$

However, these equations cannot be used to calculate the permeability-thickness product from single-well test data since r_e and p_e are unknown. Even if p_e is assumed to be equal to the initial fracture pressure p_i, the problem of properly estimating the radius of investigation r_e still remains.

We assumed r_e values of 10, 100 and 1000 m for the water injection case (Fig. 7), which yield kh estimates of 6.1, 9.1 and 12.2 D-cm respectively. Excepting the first value, the rest compare poorly with the actual value of 5 D-cm. The important point to be noted here is that for a single-well test, there is no reasonable way of guessing r_e and hence no way of calculating the conductivity. Moreover, other parameters such as the fracture width and volumetric aperture cannot be calculated even if the fracture conductivity is known. A transient test analysis, on the other hand, uses almost all of the early-time data (as opposed to only the steady state pressure), and requires a minimum number of assumptions in computing fracture properties of interest. This is demonstrated below.

Air Injection-Falloff Test Analysis

The injection test data, early time falloff data and late time falloff data are graphed in Fig. (8) through (10). The mobility thickness of the inner zone is obtained from the slope of the injection period semi-log straight line (or the falloff Horner semi-log straight line), Fig. (8) or (9)

$$\lambda_1 h = \frac{1.151 q \bar{p}}{\pi m_1} = 200 \text{ D–cm/cp}$$

The actual mobility-thickness, corresponding to an assumed average saturation of 0.555 in the invaded zone, is 210 D-cm/cp.

From the intercepts of these semi-log graphs

$$p_{wf}^2 \Big|^* = p_{wf}^2 @ \left\{ \frac{t}{r_w^2} = 1 \right\} = 1.231 \text{ atm}^2$$

$$p_{ws}^2 \Big|^* = p_i{}^2 + \frac{m_1 S}{1.151} = 0.993 \text{ atm}^2$$

the inner zone diffusivity is calculated as

$$\eta_1 = 10^{**} \left\{ \frac{p_{wf}^2 \Big|^* - p_{ws}^2 \Big|^* - 0.352 m_1}{m_1} \right\} = 805 \frac{\text{cm}^2}{\text{s}}$$

The simulator input value for this case is 820 cm^2/s.

The Horner time ratio at which the early-time semi-log straight line ends during falloff is

$$\left(\frac{t_p + \Delta t}{\Delta t} \right)^{**} \approx 10.5$$

The front velocity ratio a can be calculated from

$$a = \frac{6}{\left\{ (t_p + \Delta t)/\Delta t \right\}^{**} - 1} = 0.63$$

which leads to an estimation of the volumetric aperture

$$h_{vol} = \frac{q}{\pi a \phi \Delta s \eta_1} = 0.9 \text{ cm}$$

This compares well with the actual value of 1 cm.

The middle-time portion on the Horner graph does not produce a straight line, from which the properties of the outer zone could have been calculated. This is probably due to a near unity mobility ratio between the inner and outer zones, and the effect of the fracture lateral boundaries being felt. The average air saturation in the inner zone is 0.555, which is fairly close to the initial value of 0.50. Thus, a moving front has not really developed in the system.

The late time falloff data fall on a straight line on a square-root of time graph (Fig. 10), as is to be expected for the linear flow geometry. The intercept is equal to the square of the initial pressure 10^5 Pa, which is the same as the simulator input value.

From the slope of this straight line, the fracture width can be estimated if the mobility-thickness and diffusivity corresponding to the outer zone are known. However, since saturation changes are small, these parameters can be assumed to be roughly equal to the inner zone values. The fracture width is then calculated

$$b \approx \frac{1.128 q \bar{p}}{m_3 \lambda_1 h} \sqrt{\eta_1} = 9.6\text{m}$$

This compares well with the actual value of 10 m.

Water Injection-Falloff Test Analysis

The simulated pressure data are graphed in Fig. (11) through (14). The method of analysis is essentially the same as in the previous case, with only the substitution of appropriate dimensionless variables to develop the proper interpretive equations. See Table 4 for a definition of dimensionless variables for the liquid injection case.

From the slope of the early injection and falloff semilog graphs (Fig. 11 and 12) we obtain

$$m_1 = 0.212 \text{ atm}/\approx$$

from which the mobility-thickness of the inner zone is calculated as

$$\lambda_1 h = \frac{1.151q}{2\pi m_1} = 3.5 \text{ D-cm/cp}$$

The corresponding simulator input value is 3.8 D-cm/cp.

From the intercepts of the early-time straight lines,

$$p^*_{wf} = 1.135 \text{ atm}$$

$$p^*_{ws} = -0.0247 \text{ atm}$$

The inner zone diffusivity is then given by

$$\eta_1 = 10^{**}\left\{\frac{p^*_{wf}-p^*_{ws}-0.352\ m_1}{m_1}\right\} = 1.3 \text{ x}10^5 \text{ cm}^2/\text{s}$$

This is comparable to the simulator input value of 1.5×10^5 cm^2/s.

The time at which the early-time straight ends on the falloff graph is

$$\left(\frac{t_p+\Delta t}{\Delta t}\right)^{**} \approx 1.8 \times 10^5$$

The front velocity ratio is then calculated as

$$a = \frac{6}{\left\{\frac{(t_p+\Delta t)}{\Delta t}\right\}^{**} - 1} \approx 3.3 \times 10^5$$

The volumetric (tracer) aperture may now be estimated as

$$h_{vol} = \frac{q}{\pi\phi\Delta s a \eta_1} = 1.18 \text{ cm}$$

This compares well with the actual value of 1 cm.

The middle-time region of the fall-off graph (Fig. 13) yields a straight line with slope

$$m_2 = 3.26 \times 10^{-3} \text{ atm}/\approx$$

from which the mobility of the outer zone is given as

$$\lambda_2 h = \frac{1.151q}{2\pi m_2} = 224.8 \text{ D-cm/cp}$$

The actual value, corresponding to the initial unsaturated conditions, is 207 D-cm/cp.

The late-time fall-off data fall on a straight line on a square-root time graph (Fig. 14). The intercept is equal to the initial pressure 10^5 Pa, which is the same as the simulator input value. The slope of this straight line is

$$m_3 = 2.14 \times 10^{-4} \frac{\text{atm}}{\sqrt{\text{sec}}}$$

The fracture width can be estimated from this value if the outer zone diffusivity is known. This is estimated to be

$$\eta_2 = \frac{(\lambda_2 h)p_i}{\phi h} = 444 \frac{\text{cm}^2}{\text{s}}$$

Based on this estimate, the fracture width is calculated as

$$b = \frac{q}{m_3(\lambda_2 h)} \cdot \sqrt{\frac{\eta_2}{\pi}} = 9.75 \text{ m}$$

Discussion

It has been shown that the simple model proposed in this study gives reasonable values for many parameters of interest in fractured, unsaturated rocks. The air-injection example was approximately a unit-mobility ratio displacement case, resulting in the formation of a diffuse front. This caused problems in estimating the volumetric aperture, which could be resolved only by assuming an average value of gas saturation in the invaded zone. Such information will usually not be available. However, for highly unsaturated fractures, the problem is equivalent to single-phase gas flow, and conventional pressure analysis methods (e.g., Witherspoon et al., 1967; Earlougher, 1977) can be used to estimate fracture conductivity and width.

The assumption of a sharp moving front (i.e., piston-like displacement) will generally be true only if the invaded zone mobility is significantly less than the uninvaded zone mobility, as in the example of water injection in an unsaturated fracture containing water and air. The moving front can then be easily seen on the transient pressure response. If the original saturation is known, the volumetric aperture can be estimated

from the time at which the early-time falloff semi-log straight line ends.

If the fracture width is small, boundary effects will be felt early and may obscure the middle-time portion in the falloff data. In that case, the volumetric (tracer) aperture cannot be calculated by the method suggested in this study.

For thin fractures (which is commonly the case), even small injection rates will cause pressure gradients which are large compared to gravitational terms. This is an important observation since it facilitates the use horizontal fracture system equations to interpret inclined fracture system pressure data. Another significant finding is that the duration of elliptical flow in inclined fracture-borehole geometries is very short, and hence early-time flow may be assumed to be purely radial at all times.

One problem with gas (or air) injection is that the system response may be non-linear if pressure changes are not small. This requires a proper selection of the injection rate, so that pressure levels do not exceed 2-3 atmospheres. However, air injection is preferable from a practical standpoint as it leaves the formation mostly undisturbed. This may be an important consideration if the ultimate objective is to use the formation as a hazardous waste repository.

Conclusions

1. Analytical models for analyzing gas and water injection-falloff tests in unsaturated fractured formations have been developed. Interpretive equations to estimate fracture conductivity, width and aperture from graphical analysis of transient pressure-time data have been derived.
2. Effects of fracture inclination and gravity have been investigated numerically, and found to be negligible both for gas and water injection tests.
3. Two simulated injection tests have been interpreted using the methods presented, the results of which compare favorably with simulator input values.
4. The method of analysis suggested in this work is an alternative to conventional multi-rate gas injection tests for measuring fracture properties. Unlike

the steady-state tests, our procedure uses much of the unsteady-state data, and has the potential of providing information regarding geometrical characteristics such as fracture width and aperture.

Acknowledgements

The authors acknowledge valuable discussions with scientists from the Nuclear Hydrology Group of the U.S. Geological Survey in Denver, Colorado, especially Parviz Montazer and Dwight Hoxie. Technical review of this manuscript by Yvonne Tsang and Sally Benson of Lawrence Berkeley Laboratory is appreciated. The authors thank K. Pruess for allowing the use of TOUGH for this study. This work was carried out under U.S. Department of Energy Contract No. DE-AC03-76SF00098 via the DOE-Nevada Office in cooperation with USGS-Denver; project direction provided by W. E. Wilson.

References

Earlougher, R. C., Jr., (1977), *Advances in Well Test Analysis,* Monograph 5, Society of Petroleum Engineers, Dallas.

Grant, M. A., Donaldson, I. G., and Bixley, P. F., (1982), *Geothermal Reservoir Engineering,* Academic Press, New York City.

Horner, D. R., (1951), Pressure Buildup in Wells, Proc., Third Work Pet. Cong., Vol. II, E. J. Brill, Leiden.

Klinkenberg, L. J., (1941), The Permeability of Porous Media to Liquids and Gases, *API Drill. and Prod. Prac.,* 200 pp.

Kucuk, F., (1978) Transient Flow in Elliptical Systems, Ph.D. dissertation, Stanford University, Stanford, CA.

Muskat, M., The Flow of Homogeneous Fluids through Porous Media, IHRDC, Boston, MA 1982.

Montazer, P. M., (1982), Permeability of Unsaturated, Fractured Metamorphic Rocks Near an Underground Opening, Ph.D. thesis, Colorado School of Mines, Golden, CO.

Perrine, R. L., (1956), Analysis of Pressure Buildup Curves, *API Drill and Prod. Prac.,* 482 pp.

Pruess, K., (1985), TOUGH Users Guide, Lawrence Berkeley Laboratory Report LBL-20070, Berkeley, CA.

Ramey, H. J., Jr., (1970), Approximate Solutions for Unsteady Liquid Flow in Composite Reservoirs, *J. Cdn. Pet. Tech.,* Jan-Mar, pp. 32-37.

Trautz, R. C., (1984), Rock Fracture Aperture and Gas Conductivity Measurements In-Situ, Topical Report, Contract No. NRC-04-81-224, submitted to the U.S. Nuclear Regulatory Commission.

Witherspoon, P. A., Javandel, I., Neuman, S. P. and Freeze, R. A., (1967), *Interpretation of Aquifer Gas Storage Conditions from Water Pumping Tests,* Monograph on Project NS-38, American Gas Association, New York.

Woodward, D. K., and Thambynayagam, R. K. M., (1983), Pressure Buildup and Falloff Analysis of Water Injection Tests, unsolicited manuscript submitted to the Society of Petroleum Engineers, paper SPE 12344.

Nomenclature

a	front velocity ratio
b	fracture width (cm)
D	diffusivity ratio
h	hydraulic fracture aperture (cm)
h_{vol}	volumetric fracture aperture (cm)
k	permeability (Darcy)
m	semi-log straight line slope (atm/$\approx$)
M	mobility ratio
p	initial fracture pressure (atm)
p_{wf}	injection well flowing pressure (atm)
p_{ws}	injection well shut-in pressure (atm)
q	volumetric injection rate (cc/s)
q_m	mass injection rate (kg/s)
r	radial distance (cm)
r_w	wellbore radius (cm)
r_f	distance to front (radial flow) (cm)
Δs	saturation change in invaded zone
t_p	injection time (sec)
Δt	shut-in time (sec)
x	linear distance (cm)
x_f	distance to front (linear flow) (cm)

Greek Symbols

α	fracture inclination (degrees)
ρ	density (kg/cc)
ϕ	porosity
μ	viscosity (cp)
η	diffusivity (cm^2/s)
λ	mobility (darcy-cm/cp)
γ	constant, 1.780072

Other Expressions

Ei(-x) exponential integral, $Ei(-x) = -\int_x^\infty e^{-u}du/u$

Appendix A

Transient Pressure Response During Radial Flow

In this section, we present an analytical model describing the pressure response during the movement of a radial saturation front. Flow in the inner (invaded) and outer (uninvaded) zones is governed by the diffusivity equation

$$\frac{1}{r}\frac{\partial}{\partial r}\left(r\frac{\partial p_1^2}{\partial r}\right) = \frac{1}{\eta_1}\frac{\partial p_1^2}{\partial t} \tag{A.1a}$$

$$\frac{1}{r}\frac{\partial}{\partial r}\left(r\frac{\partial p_2^2}{\partial r}\right) = \frac{1}{\eta_2}\frac{\partial p_2^2}{\partial t} \tag{A.1b}$$

Here, subscripts 1 and 2 refer to the inner and outer zones respectively. Diffusivity η is defined as

$$\eta_{1,2} = \frac{\overline{p}\lambda_{1,2}}{\phi} \tag{A.2}$$

and the mobility λ is defined as

$$\lambda_{1,2} = \frac{k}{\mu}\bigg|_{1,2} \tag{A.3}$$

Initially, the system is in pressure equilibrium

$$p_1^2(r,0) = p_2^2(r,0) = p_i^2 \tag{A.4}$$

A line source well is injecting at a constant rate at the inner boundary

$$\frac{\pi\lambda_1 h}{\overline{p}}\left(r\frac{\partial p_1^2}{\partial r}\right)_{r\to 0} = q \tag{A.5}$$

The outer boundary is undisturbed at all times

$$p_2^2(\infty,t) = p_i^2 \tag{A.6}$$

At the moving front, both pressure and flux are continuous

$$p_1^2(r_f,t) = p_2^2(r_f,t) \tag{A.7}$$

$$\lambda_1 \left(\frac{\partial p_1^2}{\partial r}\right)_{r_f} = \lambda_2 \left(\frac{\partial p_2^2}{\partial r}\right)_{r_f} \tag{A.8}$$

The movement of the front is assumed to be piston-like, i.e., the front is modeled as a plane of constant saturation separating the injected fluid from the in-situ fluid. From material balance considerations

$$qt = \pi r_f^2 h_{vol} \phi \Delta s \tag{A.9}$$

This implies that the movement of the front is such that r_f^2/t is a constant. The set of equations (A.1) through (A.9) will be solved using Boltzman's transformation. We define two new variables

$$y = \frac{r^2}{4\eta_1 t} \tag{A.10}$$

$$x = \frac{r^2}{4\eta_2 t} \tag{A.11}$$

Substituting in Eq. (A.1), we obtain

$$y \frac{d^2 p_1^2}{dy^2} + \frac{dp_1^2}{dy}(1+y) = 0 \tag{A.12}$$

$$x \frac{d^2 p_2^2}{dy^2} + \frac{dp_2^2}{dy}(1+x) = 0 \tag{A.13}$$

Associated initial and boundary conditions are

$$p_1^2 = p_2^2 = p_i^2 \quad \text{as } y,x \to \infty \tag{A.14}$$

$$\lim_{y \to 0} 2y \frac{dp_1^2}{dy} = -\frac{q\bar{p}}{\pi \lambda_1 h} \tag{A.15}$$

$$p_1^2 = p_2^2 \text{ at } \frac{t}{r_f^2} = \varsigma^{-1} \tag{A.16}$$

$$\lambda_1 \left\{ y \frac{dp_1^2}{dy} \right\}_{y_f} = \lambda_2 \left\{ x \frac{dp_2^2}{dx} \right\}_{x_f} \tag{A.17}$$

Now integrating Eq. (A.12)

$$\frac{dp_1^2}{dy} = \frac{c_1 e^{-y}}{y} \tag{A.18}$$

The constant c_1 can be evaluated by substituting Eq. (A.18) in (A.15). This gives

$$c_1 = -\frac{q\bar{p}}{2\pi\lambda_1 h} \tag{A.19}$$

and

$$\frac{dp_1^2}{dy} = \frac{q\bar{p}}{2\pi\lambda_1 h}\,\frac{e^{-y}}{y} \tag{A.20}$$

When (A.20) is integrated, we obtain

$$p_1^2 = +\frac{q\bar{p}}{2\pi\lambda_1 h}\int_{y_f}^{y}\frac{e^{-y}}{y}\,dy + c_2 \tag{A.21}$$

where

$$y_f = \frac{r_f^2}{y\eta_1 t} = \frac{\zeta}{y\eta_1} \tag{A.22}$$

Equation (A.21) can be rearranged as

$$p_1^2 = +\frac{q\bar{p}}{2\pi\lambda_1 h}\left\{\int_{y_f}^{\infty}\frac{e^{-y}}{y}\,dy - \int_{y}^{\infty}\frac{e^{-y}}{y}\,dy\right\} + c_2 \tag{A.23}$$

The exponential integral is defined as

$$Ei\,(-x) = \int_{u}^{\infty}\frac{e^{-u}}{u}\,du \tag{A.24}$$

Then Eq. (23) gives

$$p_1^2 = +\frac{q\bar{p}}{2\pi\lambda_1 h}\left\{Ei(-y) - Ei(-y_f)\right\} + c_2 \tag{A.25}$$

In order to evaluate c_2, the pressure in the invaded zone p_2 has to be estimated. Integrating Eq. (A.13),

$$\frac{dp_2^2}{dx} = \frac{c_3 e^{-x}}{x} \tag{A.26}$$

Applying the boundary condition of Eq. (A.17), one obtains

$$c_3 = -\frac{q\bar{p}}{2\pi\lambda_2 h} \exp\left\{-(y_f - x_f)\right\} \tag{A.27}$$

where $x_f \frac{r_f^2}{\mu\eta_2 t}$. Substituting for c_3 in (A.28) and integrating

$$p_2^2 = \frac{q\bar{p}}{2\pi\lambda_2 h} \exp\left\{-(y_f - x_f)\right\} \cdot \int_x^\infty \frac{e^{-x}}{x}\, dx + c_4 \tag{A.28}$$

or,

$$p_2^2 = +\frac{q\bar{p}}{2\pi\lambda_2 h} \exp\left\{-(y_f - x_f)\right\} \cdot Ei(-x) + c_4 \tag{A.29}$$

Application of Eq. (A.14) gives

$$c_4 = p_i^2 \tag{A.30}$$

Thus, the pressure in the outer zone is given by

$$p_2^2 = +\frac{q\bar{p}}{2\pi\lambda_2 h} \exp\left\{-(y_f - x_f)\right\} \cdot Ei(-x) \tag{A.31}$$

Recall, from Eq. (A.16),

$$p_1^2 = p_2^2 \text{ when } \frac{t}{r_f^2} = \varsigma^{-1}$$

Thus, from Eq. (A.25) and (A.31),

$$c_2 = +\frac{q\bar{p}}{2\pi\lambda_2 h} \exp\left\{-(y_f - x_f)\right\} \cdot Ei(-x_f) \tag{A.32}$$

Hence, the pressure in the inner zone is given by

$$p_1^2 - p_i^2 = \frac{q\bar{p}}{2\pi\lambda_1 h}\left\{Ei(-y) - Ei(-y_f)\right\}$$

$$-\frac{q\bar{p}}{2\pi\lambda_2 h} \exp\left\{+(y_f - x_f)\right\} Ei(-x_f) \tag{A.33}$$

The wellbore being the observation point of interest, one obtains

$$p_{wf}^2 - p_i^2 = \frac{q\bar{p}}{2\pi\lambda_1 h}\left\{Ei\left(-\frac{r_w^2}{\mu\eta_1 t}\right) - Ei\left(-\frac{r_f^2}{\mu\eta_1 t}\right)\right\}$$

$$+ \frac{q\bar{p}}{2\pi\lambda_2 h} \cdot \exp\left\{-\left[\left(\frac{r_f^2}{\mu\eta_1 t}\right) - \left(\frac{r_f^2}{\mu\eta_2 t}\right)\right]\right\} \cdot Ei\left(-\frac{r_f^2}{\mu\eta_2 t}\right) \qquad (A.34)$$

We now define the followng dimensionless variables

$$p_{wD} = \left(p_{wf}^2 - p_i^2\right)\frac{\pi\lambda_1 h}{q\bar{p}} \qquad (A.35)$$

$$t_D = \frac{\eta_1 t}{r_w^2} \qquad (A.36)$$

$$M = \frac{\lambda_1}{\lambda_2} \qquad (A.37)$$

$$D = \frac{\eta_1}{\eta_2} \qquad (A.38)$$

$$a = \left(\frac{q}{\pi h_{vol}\phi\Delta s}\right)\left(\frac{1}{\eta_1}\right) \qquad (A.39)$$

Substituting in Eq. (A.34) we obtain the dimensionless injection pressure response at the wellbore

$$p_{wD} = \frac{1}{2}\left\{Ei\left(-\frac{1}{4t_D}\right) - Ei\left(-\frac{a}{4}\right)\right\}$$

$$+ \frac{M}{2}\left\{Ei\left(-\frac{aD}{4}\right) \cdot \exp\left(-\frac{a(1-D)}{4}\right)\right\} \qquad (A.40)$$

As pointed out earlier, similiar solutions have been derived for liquid flow in composite media by Ramey (1970) and Woodward and Thambynayagan (1983).

Appendix B

Pressure Transient Behavior for the Linear Flow Period

In this appendix, we present an analytical model describing the pressure response during the movement of a linear front. As in the radial flow case, the diffusivity equation governs flow in both the inner (invaded) and outer (uninvaded) zones:

$$\frac{\partial^2 p_1^2}{\partial x^2} = \frac{1}{\eta_1} \frac{\partial p_1^2}{\partial t} \tag{B.1a}$$

$$\frac{\partial^2 p_2^2}{\partial x^2} = \frac{1}{\eta_2} \frac{\partial p_2^2}{\partial t} \tag{B.1b}$$

Initially, the system is in pressure equilibrium:

$$p_1^2(x,0) = p_2^2(x,0) = p_i^2 \tag{B.2}$$

A plane source is injecting at a constant rate at the inner boundary:

$$\frac{\lambda_1 bh}{2\overline{p}} \left. \frac{\partial p_1^2}{\partial x} \right|_{x \to 0} = -\frac{q}{2} \tag{B.3}$$

The outer boundary is undisturbed at all times:

$$p_2^2(\infty,t) = p_i^2 \tag{B.4}$$

At the moving boundary, both fluid flux and pressure are continuous:

$$\lambda_1 \left. \frac{\partial p_1^2}{\partial x} \right|_{x_f} = \lambda_2 \left. \frac{\partial p_2^2}{\partial x} \right|_{x_f} \tag{B.5}$$

$$p_1^2(x_f,t) = p_2^2(x_f,t) \tag{B.6}$$

The front moves as a plane, which is expressed by the material balance condition

$$qt = bx_f h_{vol} \phi \Delta s \tag{B.7}$$

These equations are converted into dimensionless form through the use of the following dimensionless variables.

$$p_D^* = \frac{\lambda_1 h}{q\overline{p}} \left(p^2 - p_i^2\right) \tag{B.8}$$

$$t_D^* = \eta_1 \frac{t}{b^2} \tag{B.9}$$

$$x_{fD} = \frac{x_f}{b} \tag{B.10}$$

$$x_D = \frac{x}{b} \tag{B.11}$$

Mobility ratio M and diffusivity ratio D are defined to be the same as those for the radial case. This leads to the following non-dimensional set of equations

$$\frac{\partial^2 p_{D1}^*}{\partial x_D^2} = \frac{\partial p_{D1}^*}{\partial t_D^*} \tag{B.12}$$

$$\frac{\partial^2 p_{D2}^*}{\partial x_D^2} = D \frac{\partial p_{D2}^*}{\partial t_D^*} \tag{B.13}$$

$$p_{D1}^* \left(x_{D,0}\right) = p_{D2}^* \left(x_{D,0}\right) = 0 \tag{B.14}$$

$$\frac{\partial p_{D1}^*}{\partial x_D} = -1 \tag{B.15}$$

$$p_{D1}^* \left(\infty, t_D^*\right) = 0 \tag{B.16}$$

$$M \frac{\partial p_{D1}^*}{\partial x_D}\bigg|_{x_{fD}} = \frac{\partial p_{D2}^*}{\partial x_D}\bigg|_{x_{fD}} \tag{B.17}$$

$$p_{D1}^* \left(x_{fD}, t_D^*\right) = p_{D2}^* \left(x_{fD}, t_D^*\right) \tag{B.18}$$

The time-dependence is eliminated through the use of the Laplace transformation

$$\overline{p}_D^* \left(x_D, l\right) = \int_0^{t_D^*} \overline{e}^{\tau l} \; p_D^* \left(x_D, \tau\right) d\tau \tag{B.19}$$

where l is the Laplace space parameter. This yields

$$\frac{d^2 \overline{p}_{D1}^*}{dx_D^2} = l \, \overline{p}_{D1}^* \tag{B.20a}$$

$$\frac{d^2\overline{p}^*_{D2}}{dx_D^2} = l\, D\overline{p}^*_{D2} \tag{B.20b}$$

$$\overline{p}^*_{D1}\left(x_{fD}, l\right) = \overline{p}_{D2}\left(x_{fD}, l\right) \tag{B.21}$$

$$M\ \frac{d\overline{p}^*_{D1}}{dx_D}\bigg|_{x_{fD}} = \frac{d\overline{p}^*_{D2}}{dx_D}\bigg|_{x_{fD}} \tag{B.22}$$

$$\overline{p}^*_{D2}(\infty, l) = 0 \tag{B.23}$$

$$\frac{d\overline{p}^*_{D1}}{dx_D}\bigg|_{x_D \to 0} = -\frac{1}{l} \tag{B.24}$$

The general solution for Eq. (B.20) is

$$\overline{p}^*_{D1} = A_1 \exp\left(x_D\sqrt{l}\right) + B_1 \exp\left(-x_D\sqrt{l}\right) \tag{B.25a}$$

$$\overline{p}^*_{D2} = A_2 \exp\left(x_D\sqrt{l\,D}\right) + B_2 \exp\left(-x_D\sqrt{l\,D}\right) \tag{B.25b}$$

In order to satisfy Eq. (B.23), $A_2 = 0$, and hence

$$\overline{p}^*_{D2} = B_2 \exp\left(-x_D\sqrt{l\,D}\right) \tag{B.26}$$

Substituting Eqs. (B.25a) in (B.24),

$$\frac{d\overline{p}^*_{D1}}{dx_D}\bigg|_{x_{D\to 0}} = A_1\sqrt{l}\cdot\exp\left(x_d\sqrt{l}\right) - B_1\sqrt{l}\ \exp\left(-x_D\sqrt{l}\right)\ \Big|_{x_{d\to 0}} = -\frac{1}{l} \tag{B.27}$$

$$A_1 = B_1 - \frac{1}{l\sqrt{l}} \tag{B.28}$$

Substituting back in Eq. (B.25), and rearranging

$$\overline{p}^*_{D1} = B_1\left\{\exp\left(x_D\sqrt{l}\right) + \exp\left(-x_D\sqrt{l}\right)\right\} - \frac{\exp\left(x_D\sqrt{l}\right)}{l\sqrt{l}} \tag{B.29}$$

Using Eqs. (B.29) and (B.26) in Eq. (B.22), we obtain

$$M\left\{B_1\left(\sqrt{l}\ \exp\left(x_{fD}\sqrt{l}\right) - \sqrt{l}\ \exp\left(-x_{fD}\sqrt{l}\right)\right)\right.$$

$$\left. - \frac{\sqrt{l}\ \exp\left(x_{fD}\sqrt{l}\right)}{l\sqrt{l}} = -\sqrt{D}\cdot B_2 \exp\left(-x_{fD}\sqrt{D}\right)\right\} \tag{B.30}$$

which can be rearranged as

$$B_1 \left\{ M^{3/2} \left(\exp\left(x_{fD}\sqrt{l} \right) - \exp\left(-x_{fD}\sqrt{l} \right) \right) \right\}$$

$$+ B_2 \left\{ \sqrt{l^3 D} \exp\left(-x_{fD}\sqrt{l_D} \right) \right\} = M \exp\left(x_{fD}\sqrt{l} \right) \tag{B.31}$$

Similarly, Eq. (B.21) results in

$$B_1 \left\{ l^{3/2} \left(\exp\left(x_{fD}\sqrt{l} \right) + \exp\left(-x_{fD}\sqrt{l} \right) \right) \right\}$$

$$- B_2 \left\{ l^{3/2} \exp\left(-x_{fD}\sqrt{D} \right) \right\} = \exp\left(x_{fD}\sqrt{l} \right) \tag{B.32}$$

Equations (B.31) and (B.32) can be solved simultaneously to obtain the constants B_1 and B_2, which are

$$B_1 = \frac{\exp\left(x_{fD}\sqrt{l} \right) \left(M + \sqrt{D} \right)}{B_3} \tag{B.33}$$

$$B_2 = \frac{\exp\left(x_{fD}\sqrt{l\,D} \right) \left(2M \right)}{B_3} \tag{B.34}$$

where

$$B_3 = l^{3/2} \left\{ \exp\left(x_{fD}\sqrt{l} \right) \left(M + \sqrt{D} \right) - \exp\left(-x_{fD}\sqrt{l} \right) \left(M - \sqrt{D} \right) \right\} \tag{B.35}$$

The dimensionless pressures $\overline{p}^*_{D1}$ and $\overline{p}^*_{D2}$ are then given by

$$\overline{p}^*_{D1} = \frac{\left\{ 1 + \frac{M-\sqrt{D}}{M+\sqrt{D}} \cdot \exp\left(2x_D\sqrt{l} \right) \cdot \exp\left(-2x_{fD}\sqrt{l} \right) \right\}}{l^{3/2} \exp\left(x_D\sqrt{l} \right) \left\{ 1 - \frac{M-\sqrt{D}}{M+\sqrt{D}} \cdot \exp\left(2x_D\sqrt{l} \right) \right\}} \tag{B.36}$$

$$\overline{p}^*_{D2} = \frac{2M \exp\left(x_{fD}\sqrt{l\,D} \right)}{l^{3/2} \exp\left(x_D\sqrt{l\,d} \right) \left\{ \left(M+\sqrt{D} \right) \exp\left(x_{fD}\sqrt{l} \right) - \left(M-\sqrt{D} \right) \exp\left(-x_{fD}\sqrt{l} \right) \right\}} \tag{B.37}$$

At the borehole (which is the primary observation point), Eq. (B.36) reduces to

$$\bar{p}^{*}_{D1}\left(x_D=0\right)=\bar{p}^{*}_{wD}=\frac{\left\{1+\frac{M-\sqrt{D}}{M+\sqrt{D}}\exp\left(-2x_{fD}\sqrt{l}\right)\right\}}{l^{3/2}\left\{1-\frac{M-\sqrt{D}}{M+\sqrt{D}}\cdot\exp\left(-2x_{fD}\sqrt{l}\right)\right\}} \tag{B.39}$$

Since linear flow takes place only at late-times, it is useful to derive a long-time approximation from Eq. (B.38). This is given by

$$\lim_{l\to 0}\bar{p}^{*}_{wD}\approx\frac{1+\frac{M-\sqrt{D}}{M+\sqrt{D}}}{l^{3/2}\left\{1-\frac{M-\sqrt{D}}{M+\sqrt{D}}\right\}}=\frac{M}{l^{3/2}\sqrt{D}} \tag{B.39}$$

Equation (B.39) is easily inverted to yield

$$p^{*}_{wD}(t^{*}_{D})=\frac{M}{\sqrt{D}}\cdot\frac{2}{\sqrt{\pi}}\cdot\sqrt{t^{*}_{D}} \tag{B.40}$$

Appendix C

Relation between Fracture Permeability and Aperture

A relation between effective fracture permeability and aperture can be derived from hydrodynamical considerations (Muskat, 1982). A fracture of width h may be considered equivalent to an open linear channel of equal width for viscous flow conditions, the carrying capacity of such a linear channel, per unit pressure gradient, is given by

$$A = \frac{h^3}{12\mu} \tag{C.1}$$

where Q is the thruput and μ the viscosity. By equating this expression with Darcy's law, the equivalent permeability of the fracture, in cm^2, is given as

$$k = \frac{h^2}{12} \tag{C.2}$$

where h is in cm. Converting permeability to darcies, and multiplying both sides by h, one obtains

$$Kh = 8.3 \times 10^6 \, h^3 \tag{C.3}$$

which is the same as Eq. (1) of the main text.

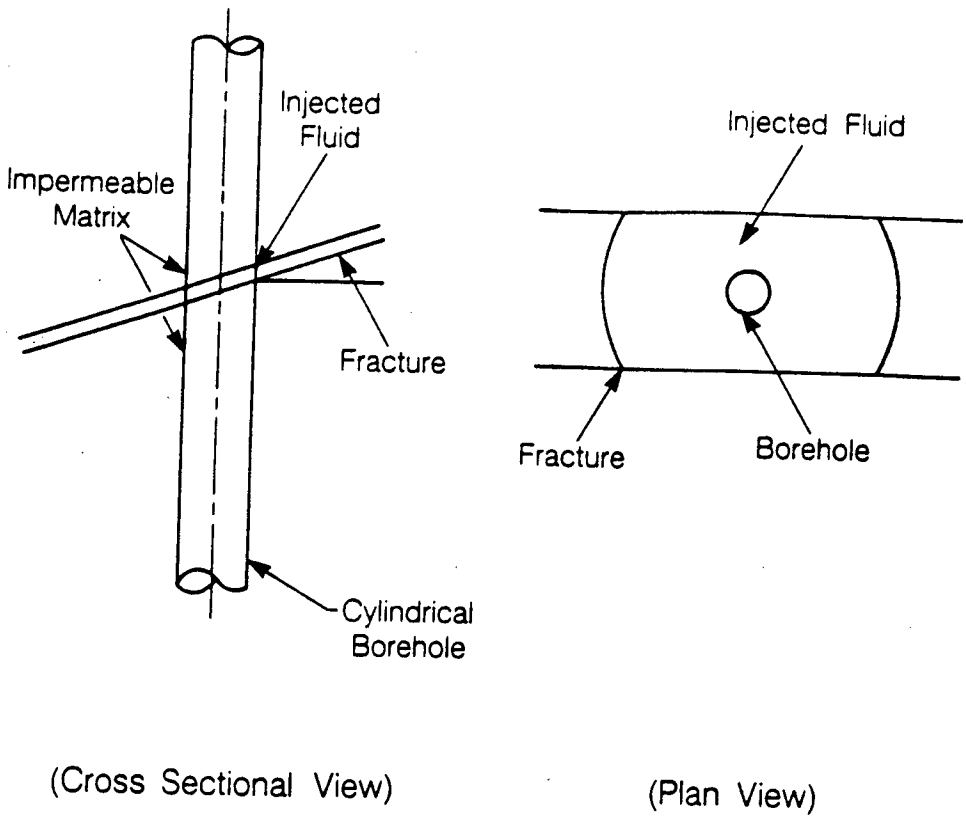

Figure 1. Schematic of physical system: (a) cross-sectional view, (b) plan view.

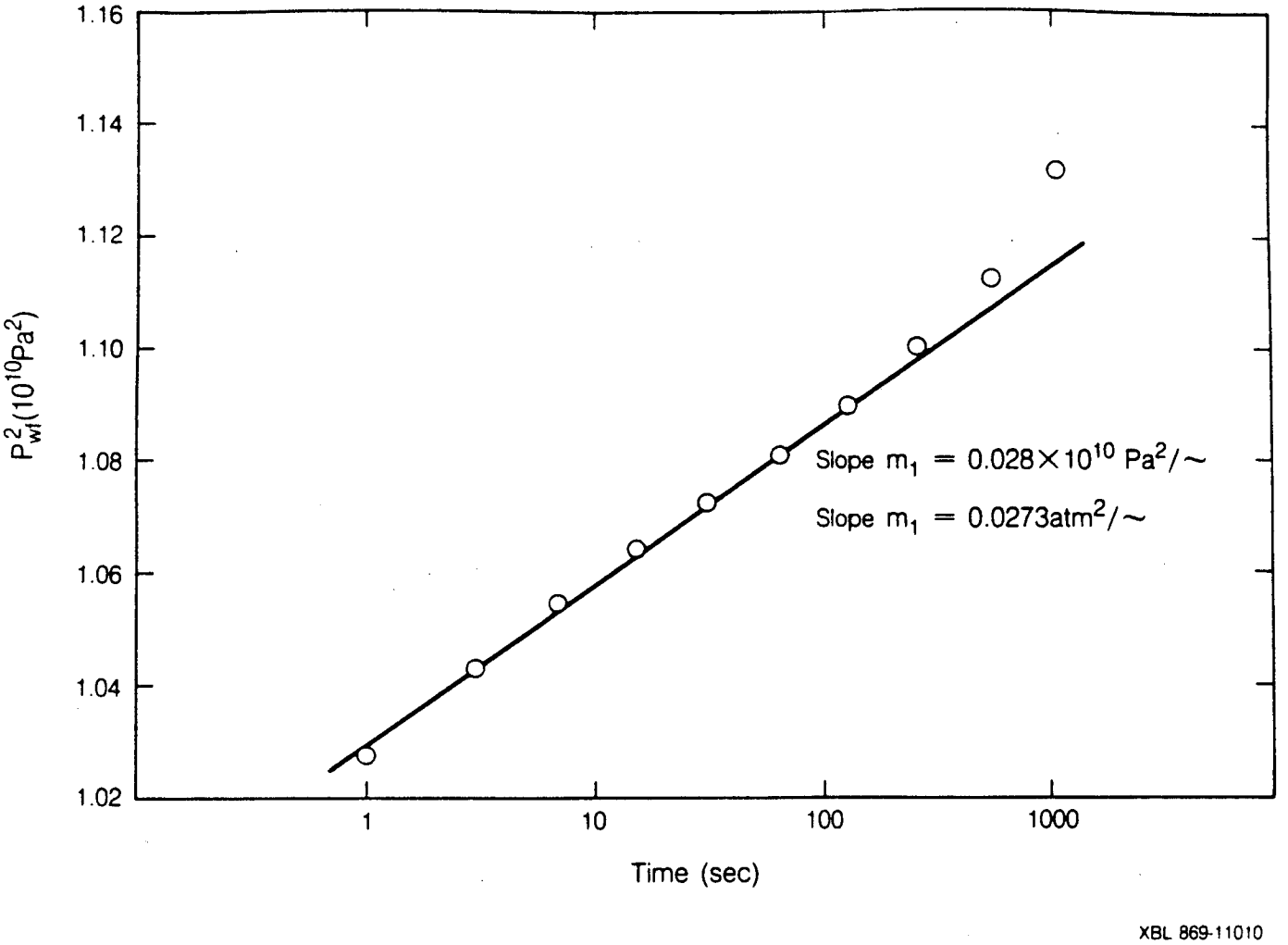

Figure 2. Linearization of gas flow equations - injection pressure data, case 1.

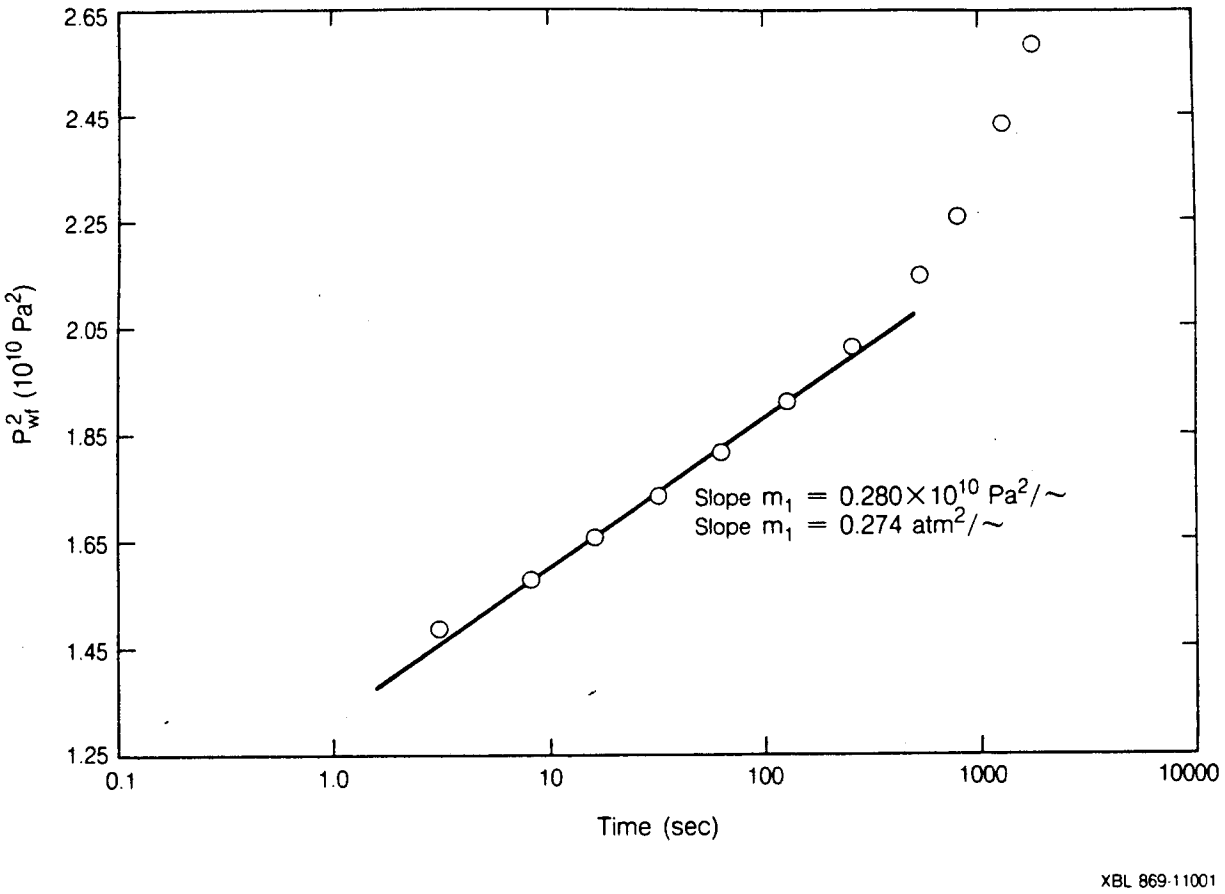

Figure 3. Linearization of gas flow equations - injection pressure data, case 2.

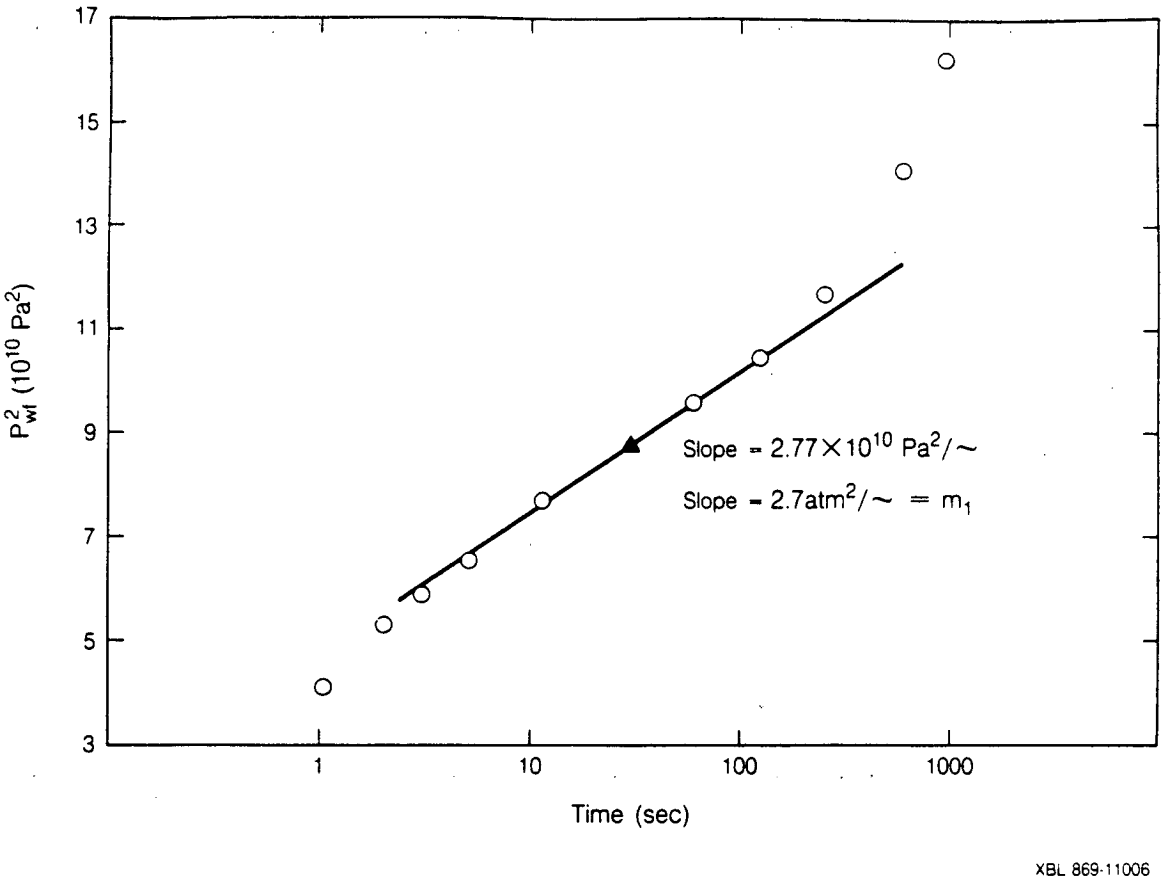

Figure 4. Linearization of gas flow equations - injection pressure data, case 3.

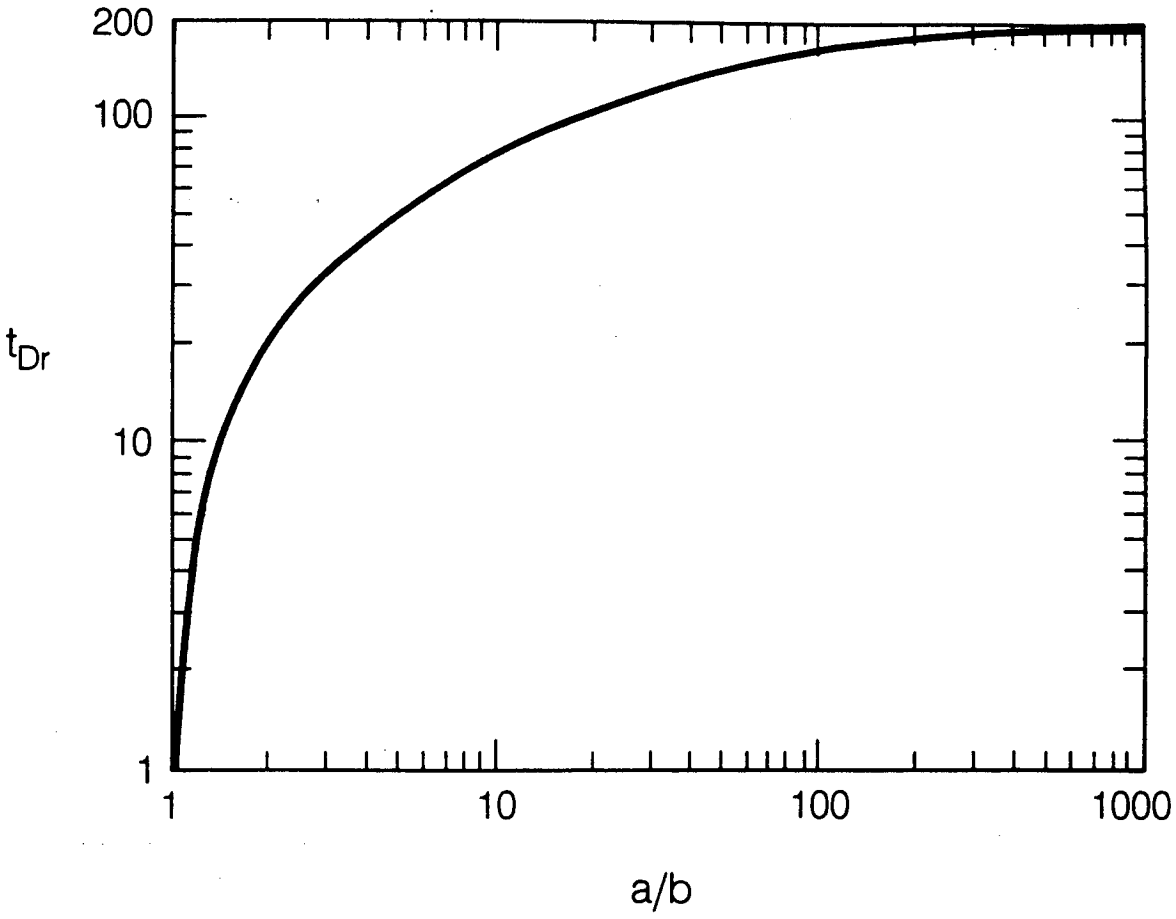

Figure 5. Dimensionless times for the onset of radial flow in elliptical flow systems (after Kucuk, 1978).

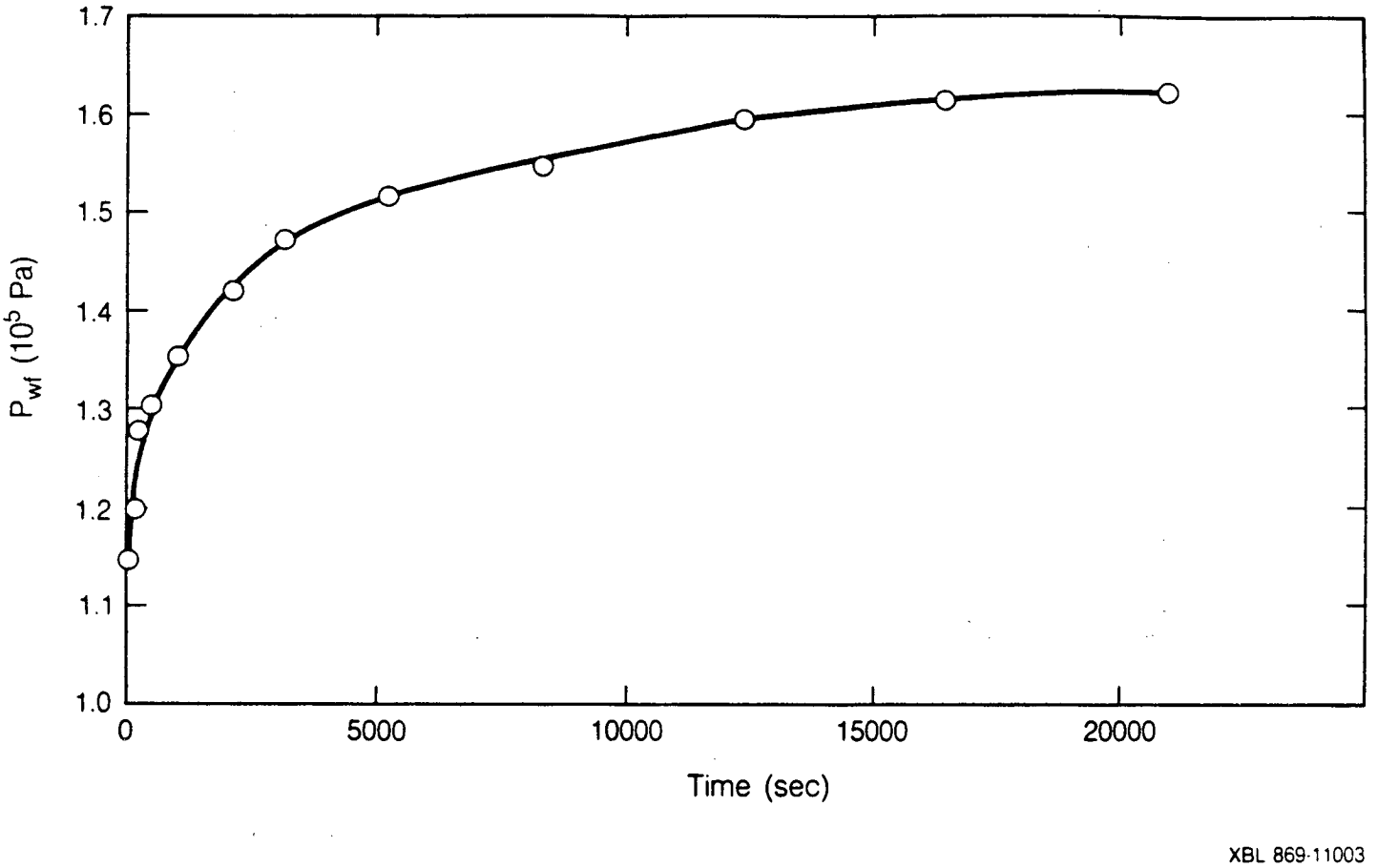

Figure 6. Cartesian graph of air injection test pressure response.

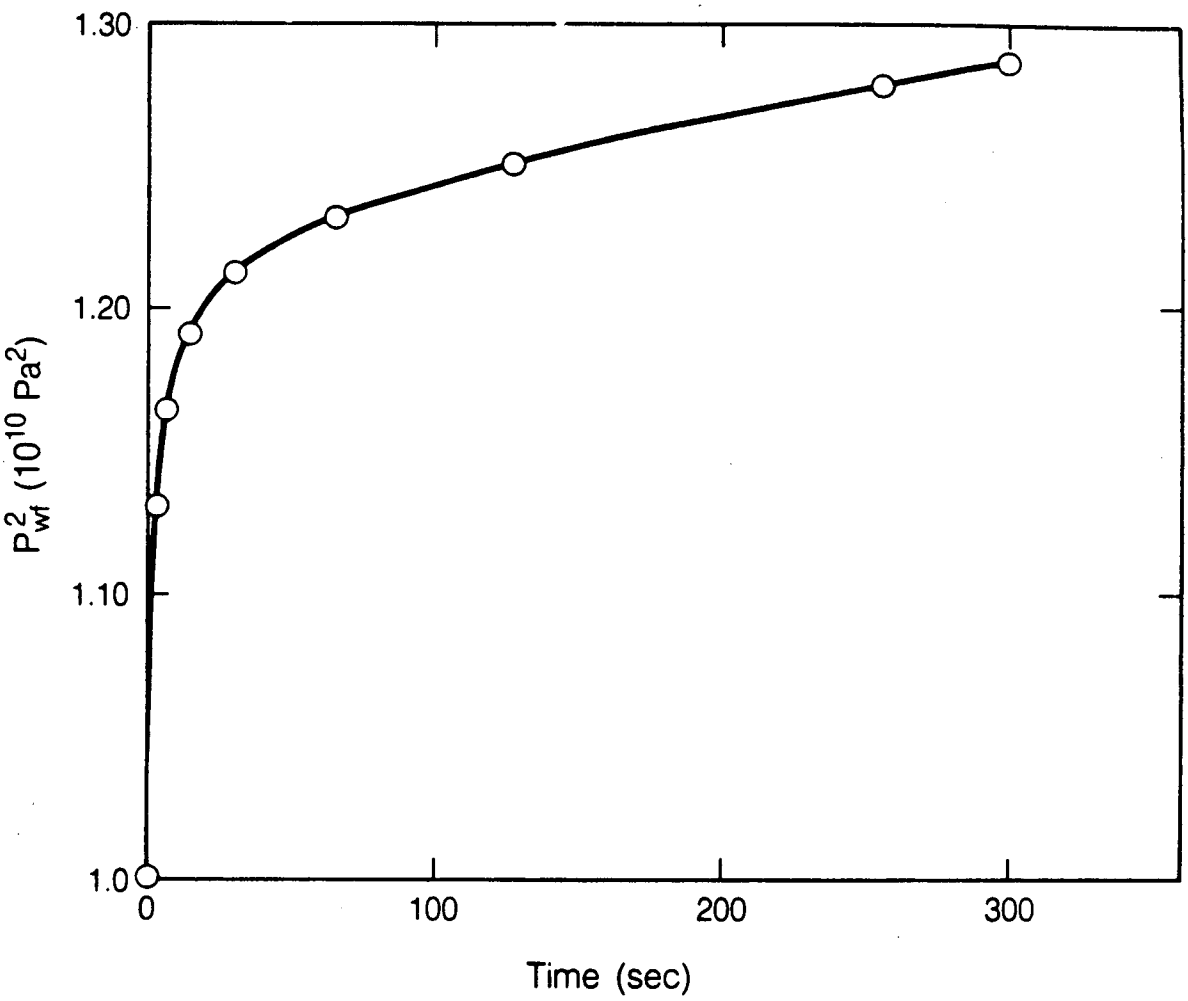

Figure 7. Cartesian graph of water injection test pressure response.

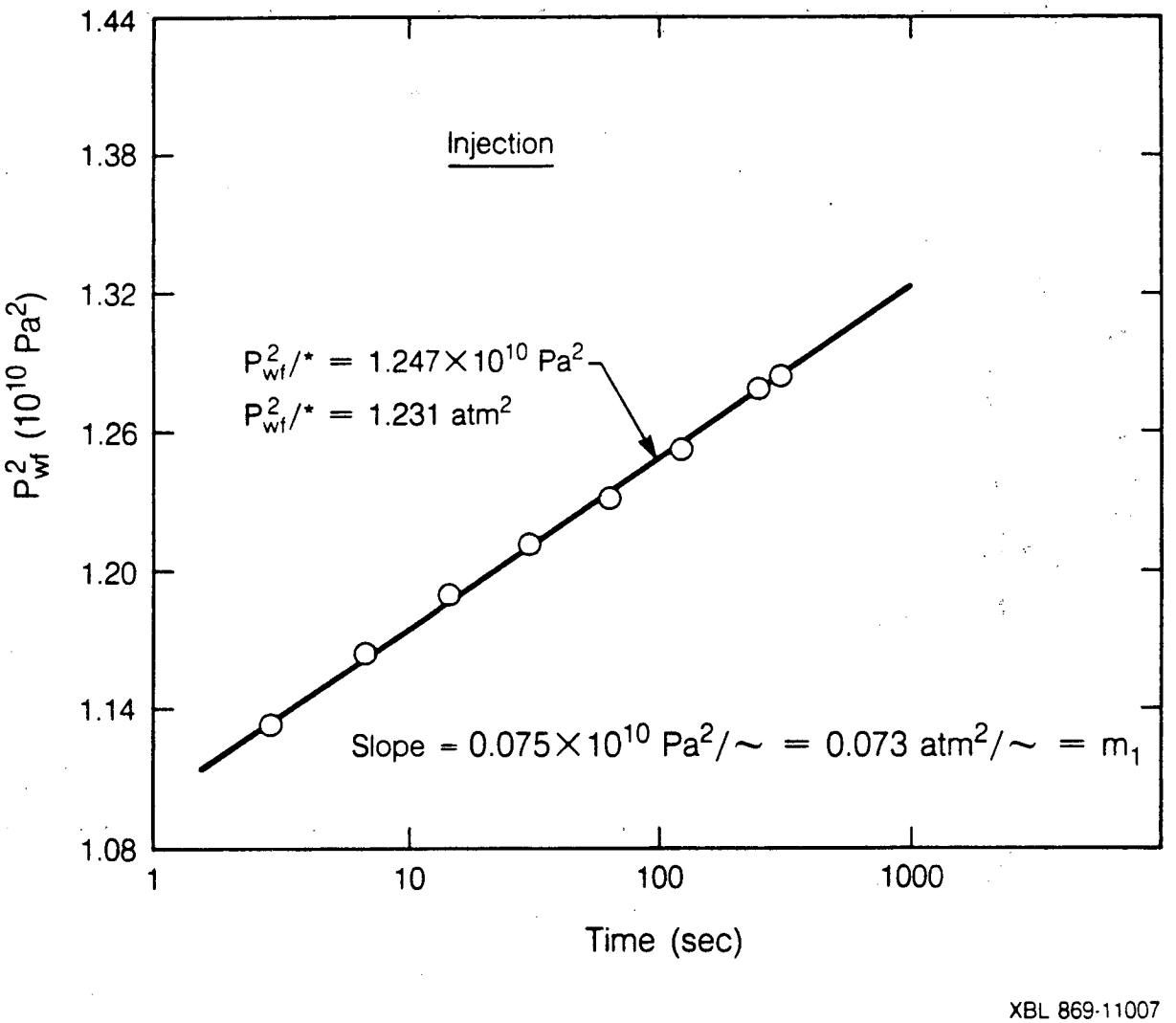

Figure 8. Semi-log graph of air injection test pressure response.

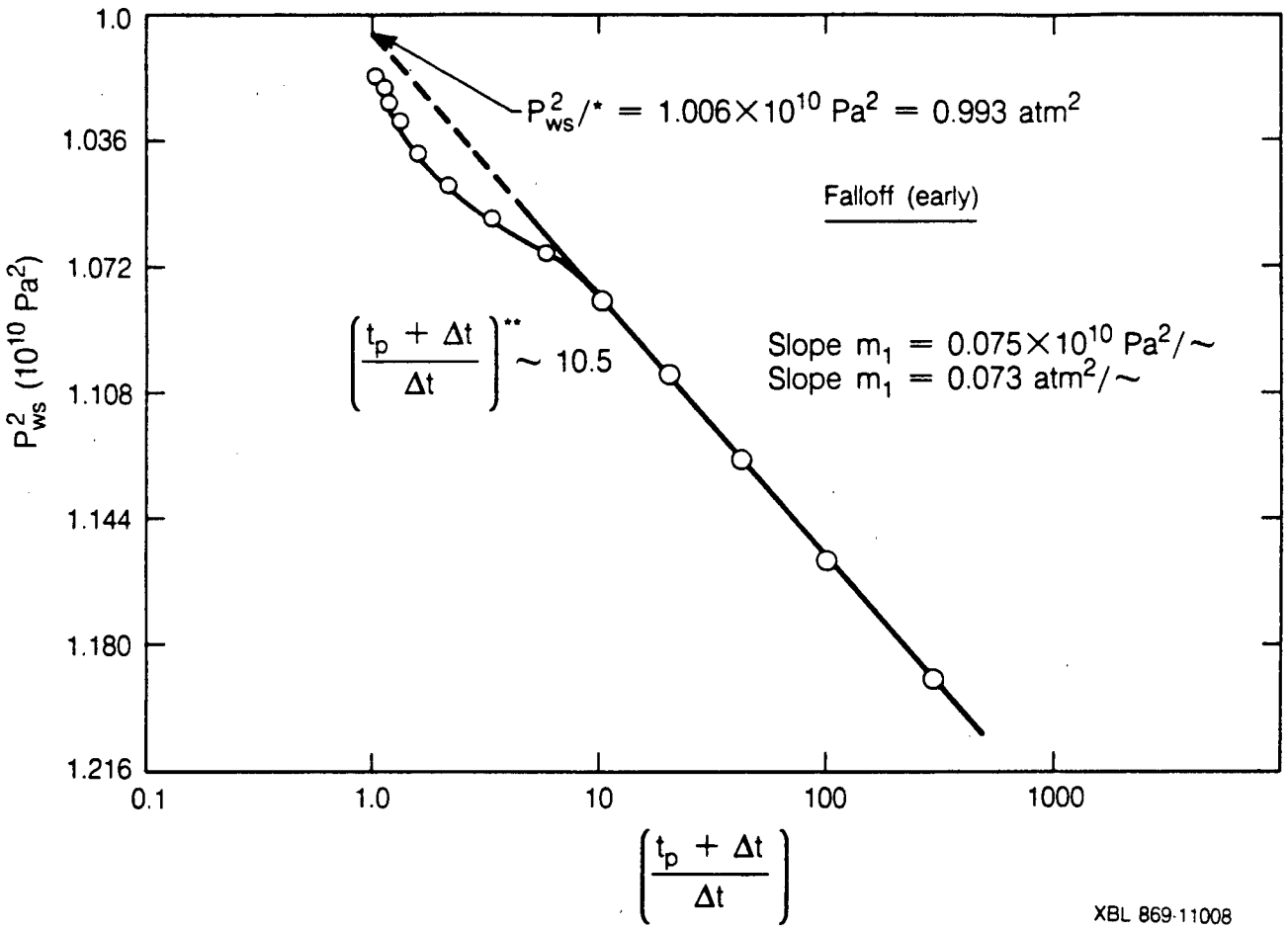

Figure 9. Horner graph of early-time falloff pressure data - air injection.

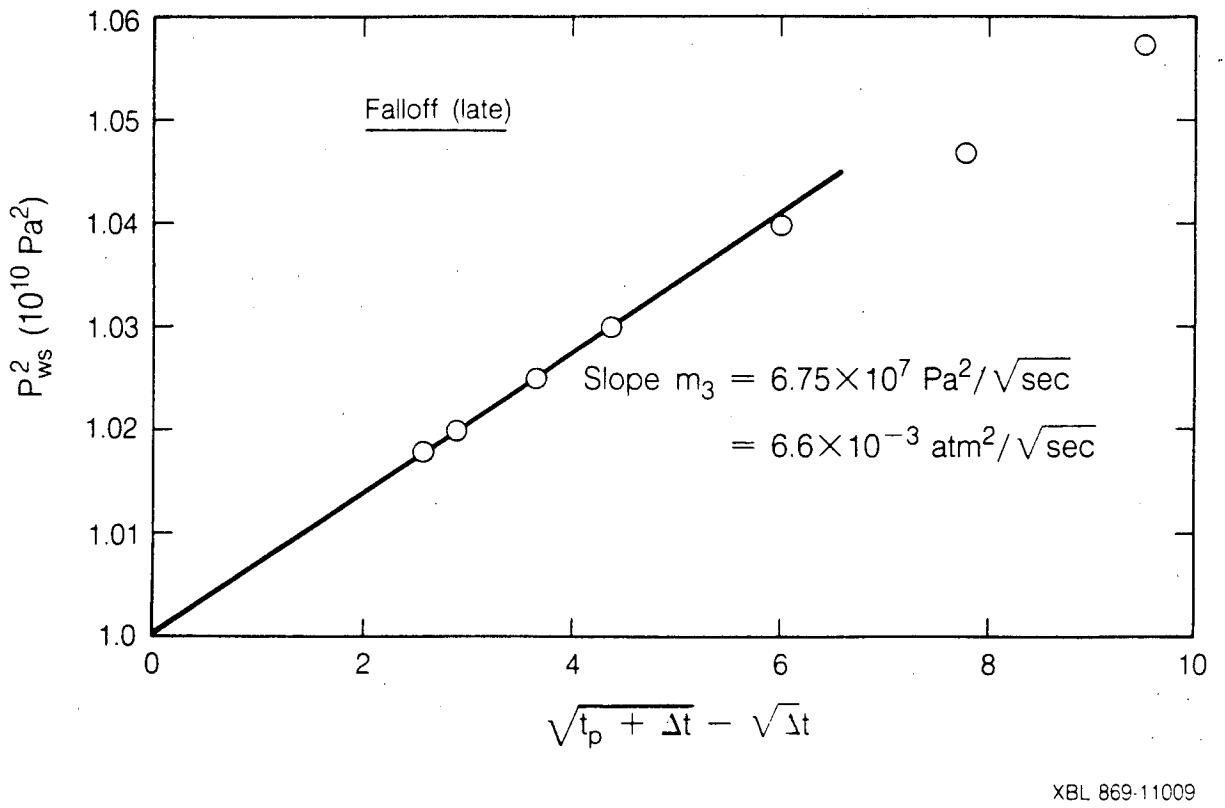

Figure 10. Square-root of time graph for late-time falloff pressure data-air injection.

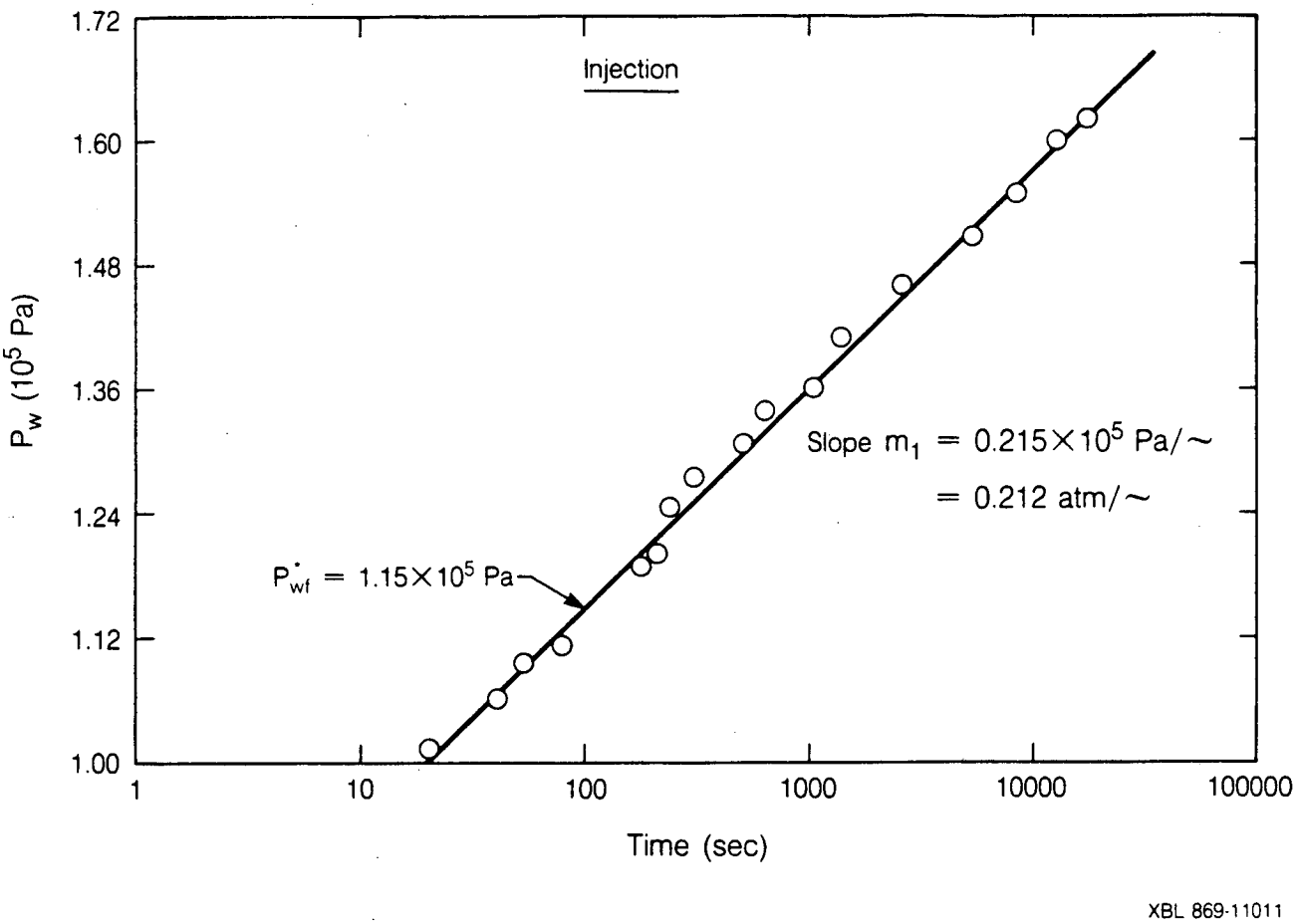

Figure 11. Semi-log graph of water injection test pressure response.

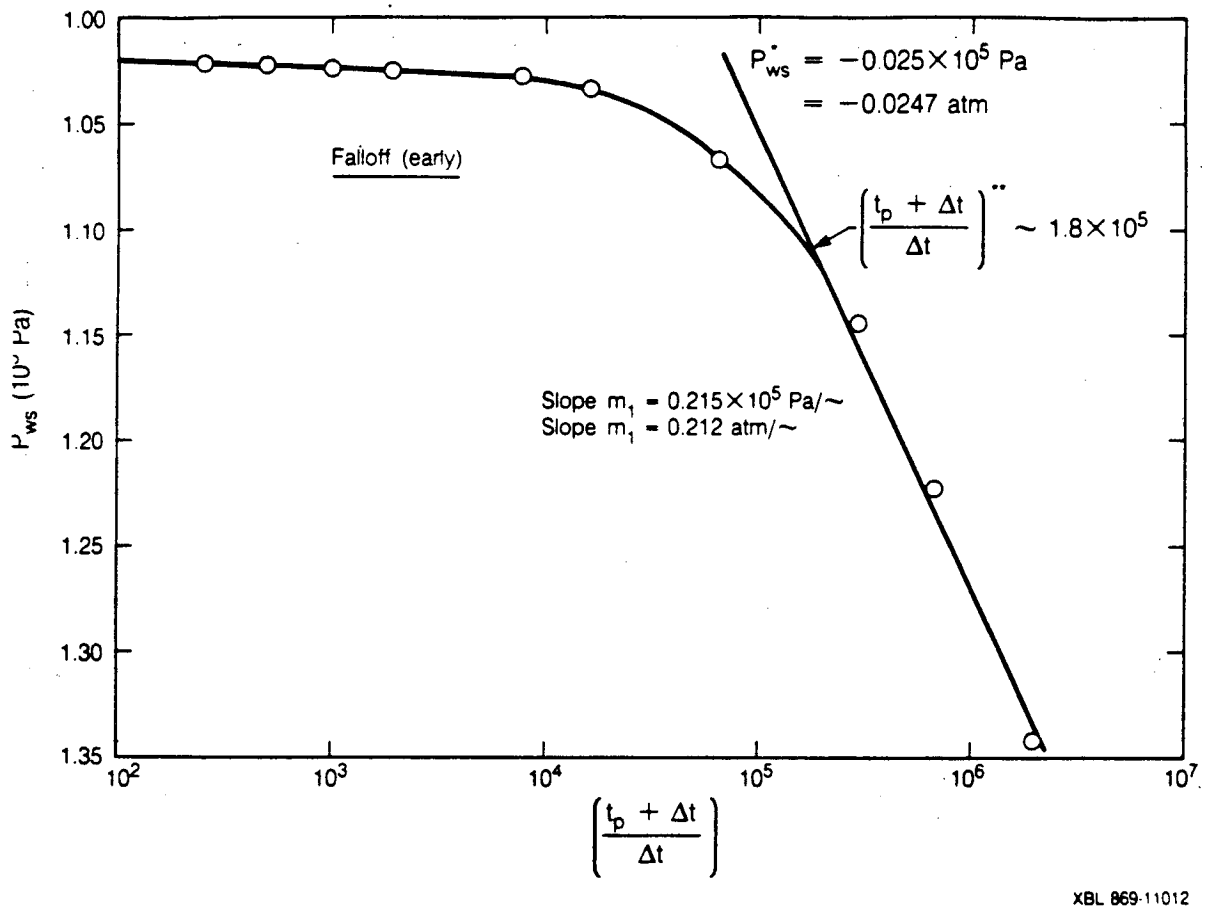

Figure 12. Horner graph of early-time falloff pressure data - water injection.

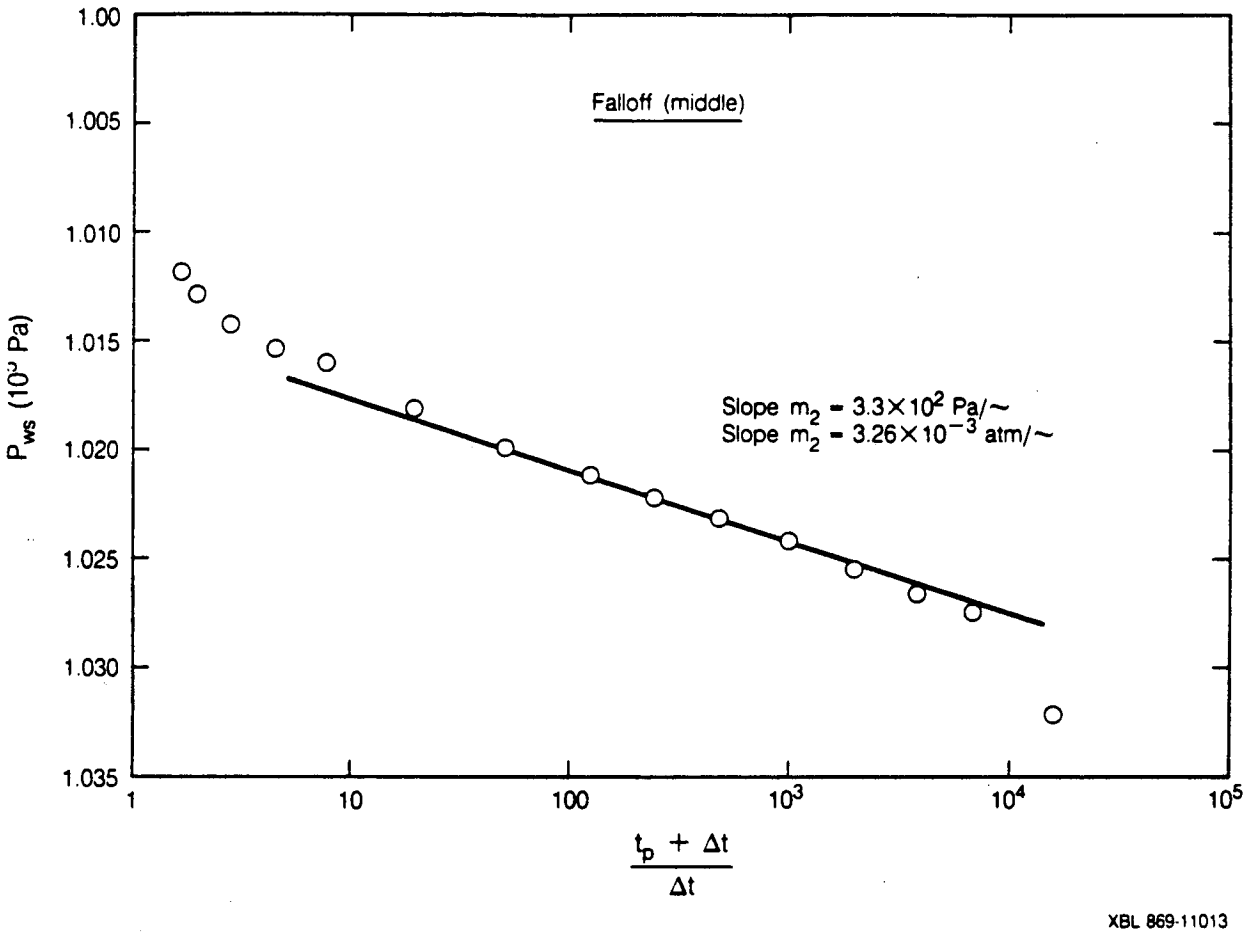

Figure 13. Horner graph of middle-time falloff pressure data - water injection.

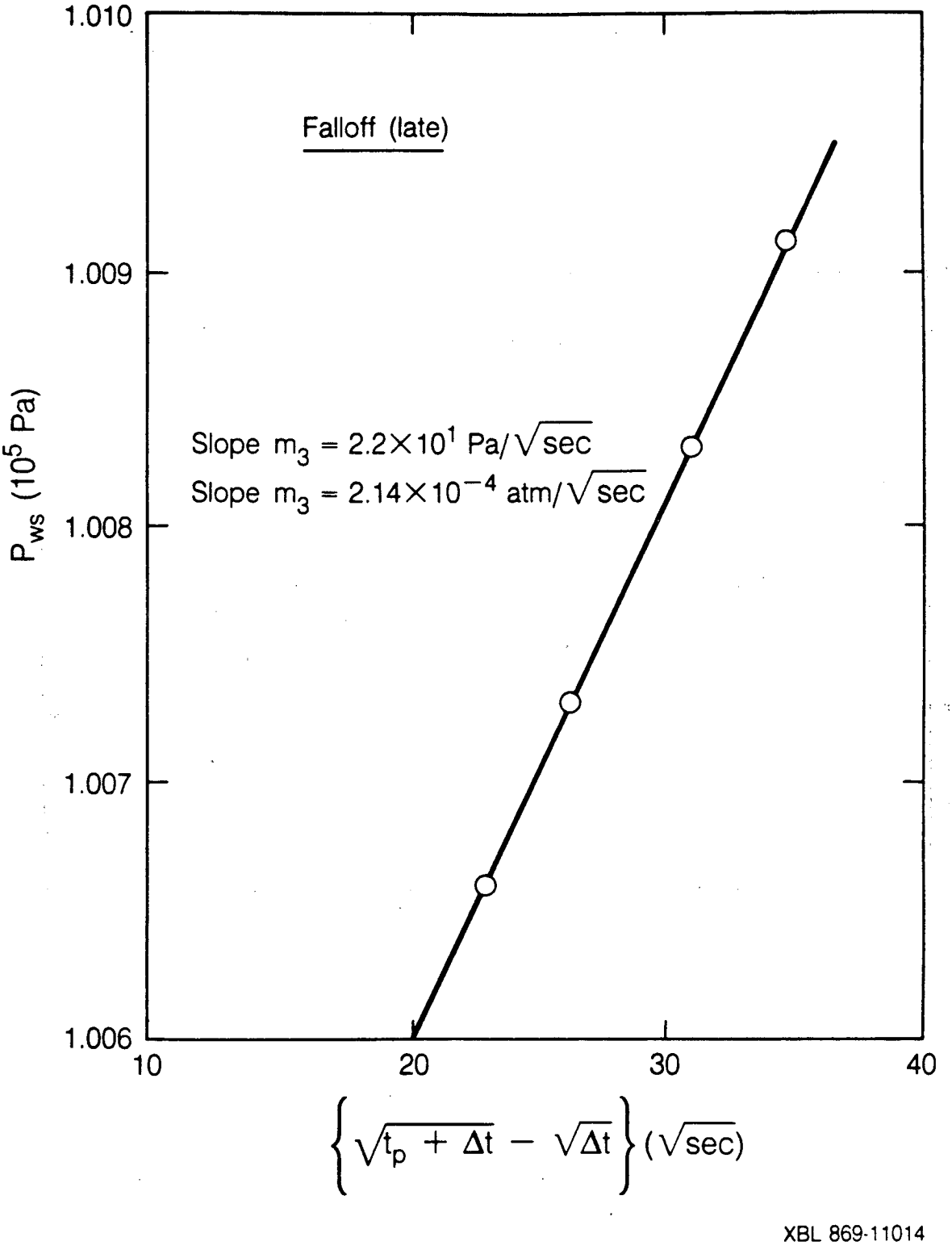

Figure 14. Square root of time graph for late-time falloff pressure data - water injection.

LAWRENCE BERKELEY LABORATORY
TECHNICAL INFORMATION DEPARTMENT
UNIVERSITY OF CALIFORNIA
BERKELEY, CALIFORNIA 94720